Mapping the cavity optomechanical interaction with sub-wavelength-sized ultrasensitive nanomechanical force sensors

Francesco Fogliano*,[1] Benjamin Besga*,[1] Antoine Reigue*,[1] Philip Heringlake,[1] Laure Mercier de Lépinay,[1] Cyril Vaneph,[2] Jakob Reichel,[2] Benjamin Pigeau,[1] and Olivier Arcizet[1]

[1] *Institut Néel, Université Grenoble Alpes - CNRS:UPR2940, 38042 Grenoble, France**

[2] *Laboratoire Kastler Brossel - UMR, Paris, France*

In canonical optomechanical systems, mechanical vibrations are dynamically encoded on an optical probe field which reciprocally exerts a backaction force. Due to the weak single photon coupling strength achieved with macroscopic oscillators, most of existing experiments were conducted with large photon numbers to achieve sizeable effects, thereby hiding the original optomechanical non-linearity. To increase the optomechanical interaction, we make use of sub-wavelength-sized ultrasensitive suspended nanowires inserted in the mode volume of a fiber-based microcavity. By scanning the nanowire within the cavity mode volume and measuring its impact on the cavity mode, we obtain a map the 2D optomechanical interaction. Then, by using the toolbox of nanowire-based force sensing protocols, we explore the back-action of the optomechanical interaction and map the optical force field experienced by the nanowire. These measurements also allow to demonstrate the possibility to detect variations of the mean intracavity photon number smaller than unity. This implementation should also allow to enter the promising regime of cavity optomechanics where a single intracavity photon can displace the oscillator by more than its zero point fluctuations, which will open novel perspectives in the field.

Introduction– The field of optomechanics has gone through many impressive developments over the last decades [1]. The coupling between a probe light field and a mechanical degree of freedom, namely an oscillator, possibly assisted by a high finesse cavity was early proposed as an ideal platform to explore the quantum limits of ultrasensitive measurements, where the quantum fluctuations of the light are the dominant source of measurement noise [2–4, 9]. The measurement backaction was also employed to manipulate the oscillator state through optical forces and dynamical backaction, leading to optomechanical correlations between both components of the system. In this framework, ground state cooling, mechanical detection of radiation pressure quantum noise, advanced correlation between light and mechanical states or optomechanical squeezing were reported [6–19]. All those impressive results were obtained in the linear regime of cavity optomechanics, making use of large photon numbers, where the interaction Hamiltonian is linearized around an operating setpoint. However, the optomechanical interaction possesses an intrinsic Kerr-like non-linearity [20] operating down to the single photon level, which has for the moment remained far from experimental reach due to the weak single photon coupling strength achieved with macroscopic oscillators.

This regime is achieved when a single photon in the cavity pushes the static rest position of the mechanical resonator by a quantity $\delta x^{(1)}$ which is larger than its zero point fluctuations δx_{zpf}. A very strong optomechanical interaction is indeed needed to fulfil this condition since it requires $g_0 > \Omega_{\mathrm{m}}$ where g_0 is the single photon optomechanical coupling and Ω_{m} the resonant angular frequency of the mechanical oscillator. The above criteria is a static (vs dynamic) metric of the interaction strength and while the terminology is not yet fully consistent across the literature, it represents a prerequisite to enter into the single-photon regime of cavity optomechanics, a major experimental challenge pursued by the community.

Depending on the relative scaling of the cavity linewidth, oscillator frequency and single photon coupling strength $(\kappa, \Omega_{\mathrm{m}}, g_0)$, different novel dynamical phenomena can be anticipated [21–32], leading for example to the possibility to observe single photon blockade [24] if the photon lifetime in the cavity is long enough ($g_0 > \kappa$) or cooling beyond the Lamb-Dicke regime. For the moment only atom-based optomechanical experiments [33, 34] could approach such a regime, while recent developments with highly deformable photonic crystals [4, 35] or trampoline [7] resonators represent interesting platforms in that perspective.

In our approach we employ sub-wavelength sized nanowires which produce significant photon scattering out of the cavity mode so that we operate in the *single photon adiabatic regime* ($\Omega_{\mathrm{m}} \ll g_0 \ll \kappa$), where the cavity field instantaneously follows mechanically induced perturbations. This regime opens perspectives for exploring the optomechanical interaction at the single mean intra-cavity photon level, which should become within experimental reach at cryogenic temperatures. It represents an interesting resource for quantum optics since the optomechanical interaction to the oscillator is sufficient to generate non-classical-states of light down to very small mean photon numbers and on a broad frequency range, not restricted to the vicinity of the mechanical resonance [9, 20]. Furthermore significant deviations from the commonly employed semi-classical description can be expected since the optical field fluctuations can have an optomechanical impact comparable to the mean field at

* equal contributions

low photon number, which should also opens the road towards the investigation of vacuum Casimir forces in confined optical resonators.

In our experiment we make use of an ultrasensitive force sensor, a suspended silicon carbide nanowire with sub-wavelength-sized diameter whose vibrating extremity is inserted in the optical mode volume of a high finesse fiber microcavity (see Fig. 1a). This "nanowire in the middle" configuration decouples mechanics from optics [8, 9, 11, 17, 38–46] and makes use of ultra-sensitive nanowires as mechanical resonators [1, 2, 5, 47, 49, 51] coupled to very short fiber Fabry-Pérot microcavities [53–55]. This experimental setup is versatile and allows us to study various aspects of the optomechanical interaction. We first explore the optical properties of the cavity field with a sub-wavelength sized probe, using scanning probe imaging techniques. We measure the dependence on the nanowire position of the resonant frequency and linewidth of the cavity mode. This allows to spatially map the parametric optomechanical coupling strength, which acquires a vectorial character due to the ability of the nanowire to vibrate along both transverse directions in the cavity mode. This exploration allows to identify locations within the cavity mode, close to the nodes, where the optomechanical coupling is maximized and where the light scattered out of the cavity mode by the nanowire, due to the enhanced light-nanowire interaction mediated by internal optical Mie resonances, has a reduced impact on the cavity linewidth. Then, we investigate the other facet of the optomechanical interaction and realize for the first time a full mapping

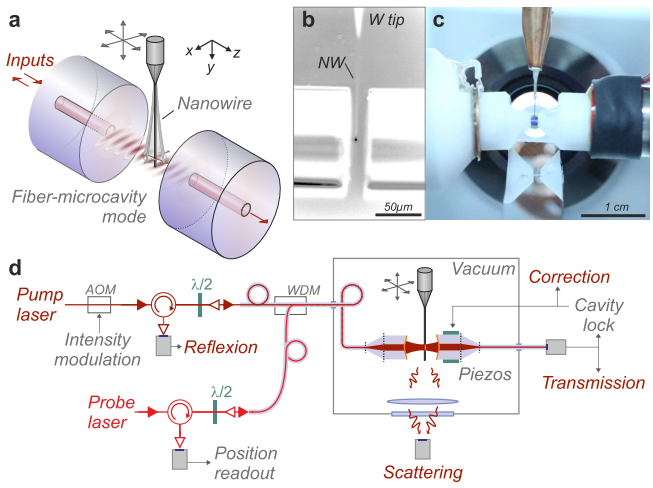

FIG. 1. **Experimental setup. a** The vibrating extremity of a silicon carbide nanowire is piezo-positioned in the optical mode volume of a high-finesse fiber microcavity to produce a large parametric coupling between the cavity optical mode and the oscillator position. **b,c** A lateral objective serves to align the experiment and collect part of the side-scattered light (dark spot in **b**). **d** Sketch of the experiment. AOM: acousto optic modulator; WDM: wavelength dividing module.

of the optomechanical force experienced by the nanowire inside the cavity mode. Those force measurements are realized using pump-probe techniques [1] operating here down to intensity modulation levels corresponding to less than one mean intracavity photon change. They provide a novel analytic tool of the intracavity field, complementary to optical measurements [55, 56].
Contrary to the case of canonical optomechanical model systems, those force measurements are essential here to fully understand the optomechanical interaction: it is not possible in general to obtain a complete knowledge of the electromagnetic field around the nanowire - and then of the optical force it experiences - from a limited set of external optical measurements (transmission/reflexion scatter channels and parametric coupling strength).
We then discuss the perspectives of this approach which allows to largely enter the emerging field of single photon and adiabatic regime of cavity optomechanics and introduce some of the phenomena that would become accessible when working with cryogenically cooled nanowires.

Formalization– The optomechanical interaction between an optical cavity mode and a single mechanical vibration mode (pulsations ω_0 and Ω_m ; ladder operators $\hat{a}, \hat{a}^\dagger$ and $\hat{b}, \hat{b}^\dagger$ respectively) is canonically described by the coupling Hamiltonian $H_\mathrm{int} = \hbar g_0 \hat{a}^\dagger \hat{a}(\hat{b} + \hat{b}^\dagger)$, which formalizes the parametric dependence of the optical cavity resonance pulsation $\omega_0(\hat{x})$ on the oscillator position $\hat{x} = \delta x_\mathrm{zpf}(\hat{b} + \hat{b}^\dagger)$, where $\delta x_\mathrm{zpf} = \sqrt{\hbar/2M_\mathrm{eff}\Omega_\mathrm{m}}$ is the spatial spreading of the oscillator zero point fluctuations (effective mass M_eff). The single photon parametric coupling strength $g_0 = \partial_x \omega_0 \, \delta x_\mathrm{zpf}$ is maximum for oscillators featuring large zero-point fluctuations - motivating the shift towards ultralight nanowires - interacting with small mode volume cavity modes. For a purely parametric coupling, a single photonic excitation ($\langle \hat{a}^\dagger \hat{a} \rangle = 1$) generates an optical force of $F^{(1)} = -\hbar g_0 / \delta x_\mathrm{zpf}$ which causes a static displacement of $\delta x^{(1)} = F^{(1)}/M\Omega_\mathrm{m}^2 = -2g_0/\Omega_\mathrm{m} \; \delta x_\mathrm{zpf}$. As such, a single intracavity photon can be expected to have an appreciable impact on the oscillator state when $\delta x^{(1)} > \delta x_\mathrm{zpf}$, which requires $g_0 > \Omega_\mathrm{m}/2$. In presence of position dependent optical losses (dissipative coupling) the magnitude of the force may differ from the above expression, which underlines the importance to spatially map of the optical force experienced by the oscillator.

Furthermore, this static deformation will in turn parametrically shift the cavity resonance, by a quantity $\delta\omega^{(1)} = g_0 \, \delta x^{(1)} / \delta x_\mathrm{zpf}$. If it exceeds the cavity linewidth, $\delta\omega^{(1)} > \kappa$, the system can thus present a static optomechanical non-linearity (bistability here) at the single intracavity photon level. Its observability thus requires large single photon parametric cooperativities, $\mathcal{C}^{(1)} \equiv 2g_0^2/\Omega_\mathrm{m}\kappa > 1$.

Up to now the achieved single photon coupling strength g_0, remained too faint to have any impact of a single photon on the oscillator state and all experiments were thus realized with large photon numbers to enhance the optomechanical interaction. In that situation, the system dynamics can be described by the linearized Hamiltonian: $\hbar g_0 \bar{\alpha} \left(\delta\hat{a} + \delta\hat{a}^\dagger\right)\left(\hat{b} + \hat{b}^\dagger\right)$, where the effective coupling strength $g_0\bar{\alpha}$ is formally enhanced by the mean intracavity field $\bar{\alpha}$. However, by doing so the fundamental optomechanical non-linearity - the optomechanically induced optical dephasing is proportional to the intracavity intensity like in the Kerr effect - gets diluted, and the regime of single photon optomechanics has remained for the moment out of experimental reach. Our approach is based on sub-wavelength sized nanowires hosting internal optical Mie resonances [8, 57] which enhances the light-nanowire interaction, inserted in small mode volume micro-cavities allows us to achieve extremely large optomechanical interaction, at the condition to precisely micro-position the nanowire extremity within the intracavity field. This thus requires a careful analysis of the spatial structure of the optomechanical interaction, which is a central report of this article.

The experiment– The fiber microcavity is made of two single-mode fibers with concavely laser machined extremities covered with high reflectivity dielectric coatings ($\approx 28\,\mu$m radii of curvature) [59]. The optical finesse can be adjusted from 400 to 45 000 by tuning the laser wavelength from 760 nm to 820 nm. The cavity geometry (fiber angles, lateral position and coarse axial length) is adjusted using motorized supports, while the cavity length can be finely tuned using a set of piezo elements for fast and slow actuation (see SI). To minimize the optical mode volume, we operate with cavity lengths down to $10\,\mu$m - which still allows to safely insert the nanowire between the fibers (see Fig. 1ab) - producing an optical cavity waist of $w_0 \approx 1.8\,\mu$m. Our nanomechanical probes are silicon carbide nanowires[1, 2, 5, 49], mounted on sharp metallic tips, whose vibrating extremity can be finely positioned within the cavity mode using an XYZ piezo stage. The employed nanowires oscillate in the 10-100 kHz range, with effective masses around 1 pg, and sub-wavelength sized diameters (100-200 nm). The experiment is conducted in static vacuum (below 10^{-2} mbar), where quality factors around 5000 are achieved, in a suspended vacuum chamber to avoid vibrations and thermally insulated to improve its long term stability. The micro-cavity is pumped by a low-noise tunable infrared Ti:saphire laser. We record the transmitted and reflected signals, but also the side-scattered photons, which are collected through a laterally positioned microscope objective (see Fig. 1cd). A digital feedback loop acting on the cavity piezos allows to lock the cavity length on resonance.

Optomechanical coupling strength– We first determine the parametric optomechanical coupling strength by measuring the dependence of the cavity resonance $\omega_0(\mathbf{r})$ on the nanowire position $\mathbf{r}$. To do so we scan the cavity length with the slow piezo stack around a mean value of $L = 12\,\mu$m and insert the nanowire in the optical mode volume. Fig. 2a represents the cavity transmission recorded when pumped at 767 nm in the vicinity of a TEM_{00} mode while scanning a 130 nm-thick-nanowire across the optical mode volume (along $\mathbf{e_x}$). This causes a cavity frequency shift, a modification of its linewidth and a change of the resonant transmission level. The nanowire diameter being much smaller than the optical wavelength, one recognizes here the lateral gaussian shape of the TEM_{00} cavity mode, with a fitted optical waist of $1.8\,\mu$m. When fully inserted (below the optical axis), the nanowire parametrically shifts the resonant cavity length by $\Delta L = -12$ nm, corresponding to an equivalent frequency shift of $\Delta\omega_0 = -\omega_0\,\Delta L/L = 2\pi \times 400$ GHz. It corresponds to a 10^{-3} relative cavity shift, in agreement with the relative increase of the optical mode volume (see SI). Similar measurements can be realized while scanning the nanowire along the optical axis ($\mathbf{e_z}$), see Fig. 2c, revealing the standing wave structure of the cavity mode, with $\lambda/2$ periodicity. When the nanowire is positioned on a node of the optical mode, the cavity field remains almost unperturbed.
Those measurements allow to spatially map the parametric coupling strength. Since the nanowire can move identically along both transverse (xz) directions, it is necessary to adopt a vectorial coupling strength $\mathbf{G} \equiv \boldsymbol{\nabla}\omega_0|_{\mathbf{r_0}}$, which has to be evaluated at the nanowire rest position $\mathbf{r_0}$. The maximum slopes observed amount to $G_x/2\pi \approx 0.3$ GHz/nm and $G_z/2\pi \approx 3$ GHz/nm. Those measurements were realized with a nanowire featuring zero-point-fluctuations spreading over $\delta r_{\mathrm{zpf}} = \sqrt{\hbar/2M_{\mathrm{eff}}\Omega_{\mathrm{m}}} \approx 0.4$ pm, so that the single photon vectorial coupling strength ($\mathbf{g_0} \equiv \mathbf{G}\ \delta r_{\mathrm{zpf}}$) is as large as $g_0^z/2\pi = 1.2$ MHz. This value, already rather large compared to other implementations [1], is significantly larger than the nanowire fundamental frequency ($\Omega_{\mathrm{m}}/2\pi = 50$ kHz here), thus largely entering the single photon regime of the parametric interaction ($g_0/\Omega_{\mathrm{m}} = 25$). The maximum linewidth broadening caused by the nanowire thermal noise [4], spreading over $\Delta r^{\mathrm{th}} = \sqrt{k_B T/M_{\mathrm{eff}}\Omega_{\mathrm{m}}^2} \approx 7$ nm amounts to $G_z\Delta r^{\mathrm{th}} \approx 2\pi \times 23$ GHz at 300K which becomes comparable to the broadened optical resonance (see Fig.2b) but remains small compared to the observed parametric shift (400 GHz).

Nanowire based characterization of the intracavity field– In view of its sub-wavelength sized diameter, the nanowire can be used to map the intracavity mode structure. Due to the finite laser mode-hop-free tunability ($\approx$ 30 GHz), we chose to lock the cavity on the laser wavelength and thus compensate the nanowire induced optical resonance shift with the cavity piezos. The error signal is synthesized from the cavity transmission signal using a 250 kHz lock-in. We use a dual feedback loop acting on the fast and slow piezo elements with a bandwidth intentionally restricted to a few kHz in order not to compensate for resonant mechanical vibrations of the

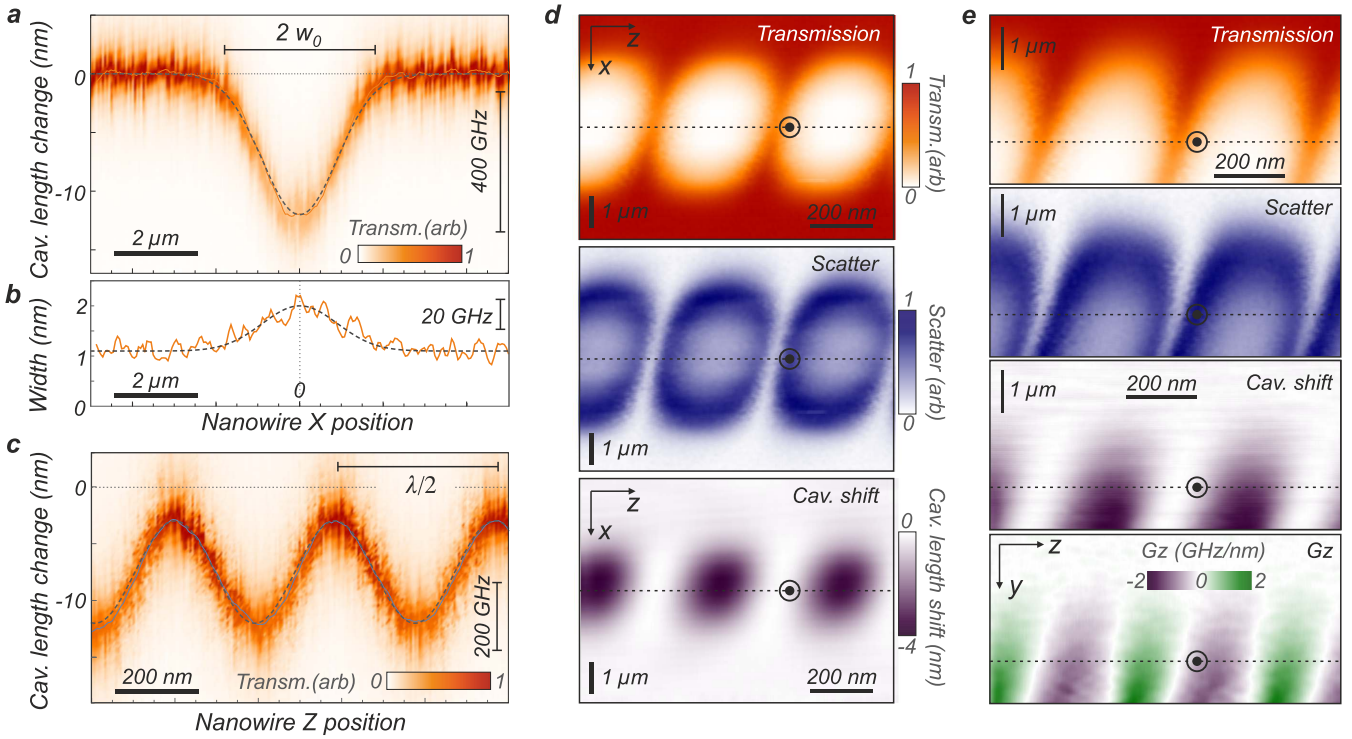

FIG. 2. **Nanowire based scanning probe exploration of the intracavity field.** **a** Transmission stack of the cavity measured while scanning its total length with the slow piezo, in the vicinity of a TEM_{00} mode and moving the nanowire across the optical mode (x axis). The dashed line is a gaussian fit of the measured resonance length shifts (1.8 μm waist). The change in linewidth is reported in b. **c** Similar measurement realized while scanning the nanowire along the optical axis, revealing the standing wave structure of the cavity mode. **d** Transmission, scatter maps measured when scanning the nanowire in the horizontal XZ plane while locking the cavity on resonance. The cavity length shift map is obtained via the correction of the feedback loop, after substraction of the slow experimental drift. **e** Similar measurements obtained when scanning the nanowire in the vertical YZ plane (X=0), the optical axis is marked with a dashed line. The parametric coupling strength G_z is obtained by spatial derivation of the cavity shift map along $\mathbf{e_z}$.

nanowire. Fig. 2d(e) represents the experimental transmission, scatter (laterally collected through the objective) and correction signals recorded when scanning the nanowire in the horizontal XZ (vertical YZ) plane. This permits a direct visualization of the intracavity standing wave, as revealed in the transmission maps. The intracavity nodes (anti-nodes) appear as regions of large (low) transmission.

The scatter maps reflect a different behavior. Progressively inserting the nanowire in the cavity mode, closer to an anti-node, first causes an increase of the scattered light, as expected. However, this is followed by a reduction (white central areas), which simply originates from the reduction of the cavity finesse due to the increased loss rate. This transition from a nanowire scattering rate smaller or larger than the bare cavity loss rate is responsible for the ring shapes observed in Fig. 2d. The same considerations also explain the signatures observed on the vertical maps, where the dispersive and dissipative optomechanical coupling rates can be tuned by adjusting the vertical insertion of the nanowire extremity in the cavity mode. As long as the nanowire stays out of a scatter ring, the cavity finesse remains almost unchanged. Interestingly, positions on each side (along $\mathbf{e_z}$) of the optical nodes where the cavity finesse remains almost unchanged also feature large parametric coupling strength, as shown in Fig. 2e (panel G_z) and are where the largest optomechanical backaction can be expected.

Those multi-channel scanning probe maps are impacted by several parameters, such as the nanowire diameter, laser wavelength and polarization, the cavity geometry (curvature, length, alignment) and finesse. They can all be tested quantitatively through this approach, which thus presents a unique interest to investigate the intracavity field in confined microcavities.

Nano-optomechanical investigation of the intracavity force– The above measurements allowed to investigate how the oscillator perturbs the intracavity field, which represents one facet of the optomechanical interaction. To fully quantify an optomechanical system it is essential to characterize the second facet of the interaction and measure the action of the intracavity light field on the oscillator. This dual characterization is essential, in

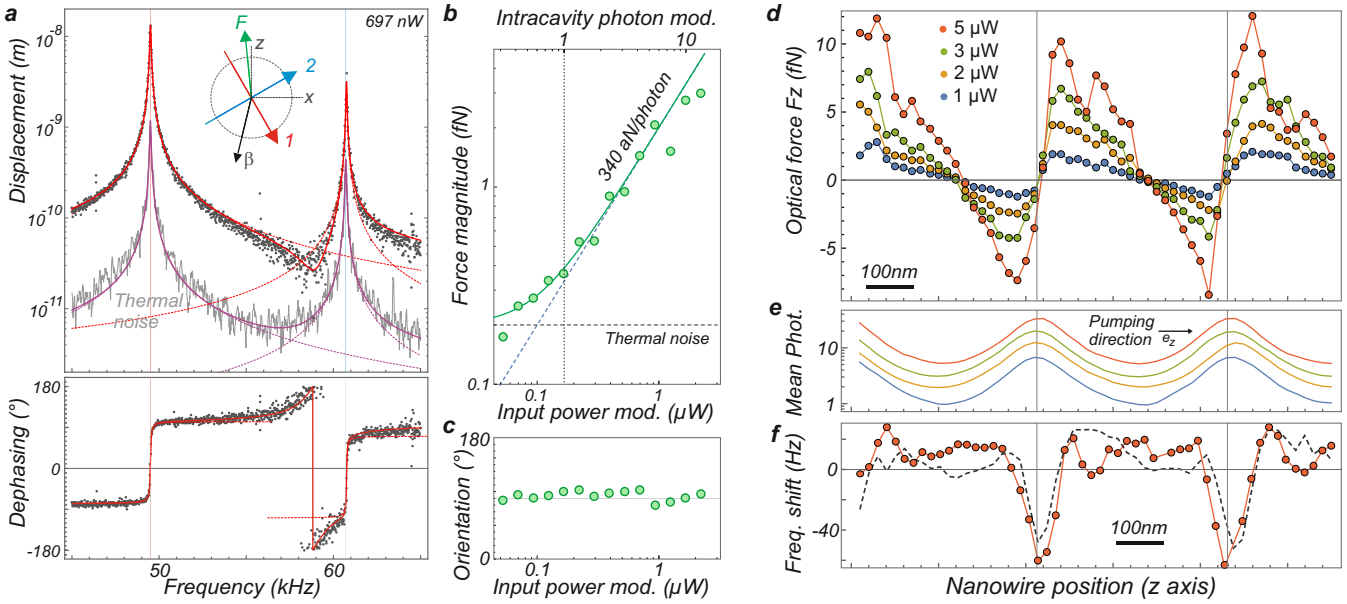

FIG. 3. **Nanomechanical measurement of the intracavity optical force. a** Thermal noise (gray line, 30 Hz resolution bandwidth) and response measurements (dots) measured with the red probe laser (5 μW) providing a projective measurement of the nanowire vibrations along the $\mathbf{e}_\beta$ axis (inset), for a cavity locked at resonance at position $\odot$ in Fig. 2de. The response measurements are realized with a vectorial network analyzer, whose output channel serves to intensity modulate the infrared cavity pump laser. The phase difference is measured between the recorded displacement and the generated intensity modulation. Fitting of the data (see text) allows to determine the eigenmode orientations $\mathbf{e_{1,2}}$, and the instantaneous optical force vector. **b,c** Evolution of the magnitude and orientation (with respect to $\mathbf{e_x}$) of the optical force vector plotted with respect to the amplitude of the intracavity photon number modulation ($\delta\langle a^\dagger a\rangle$), down to unity, and to the corresponding input power modulation amplitude (using $P_0 = 3\,\mu$W, which corresponds to 17 intracavity photons at that position, see SI). **d** Dependence of the instantaneous force F_z with the position along the optical axis for increasing input powers (70 % modulation depth). The nodes of the electromagnetic modes are indicated as vertical lines and correspond to maxima in the transmission plots shown in **e**, expressed in term of mean intracavity photon number. **f** Measured relative frequency shifts (dashed lines) obtained for 5 μW compared to the shifts expected from the measured optical force field gradients $\frac{-1}{2\Omega_m M_{\rm eff}}\partial_z F_z$ (red dots).

particular for the "oscillator in the middle" approaches when the nature and excitation level of the optical mode involved in the interaction Hamiltonian (described by the $\hat{a}$, $\hat{a}^\dagger$ operators) strongly depends on the oscillator position (optical mode spatial profile, oscillator induced losses...) and on the pumping conditions. We show here that the large force sensitivity of the nanowire combined with the large coupling strength achieved to the small mode volume microcavity mode, allows us to detect optical forces corresponding to modulations of the mean intracavity photon number smaller than unity.

We measure the intracavity force field using a pump-probe scheme [1] realized by modulating the intracavity intensity at frequencies close to the mechanical resonances, while recording the laser driven nanowire trajectories with a separate probe laser.

The visible probe laser (few μW at 633 nm falling outside of the microcavity coating reflection window) is co-injected in the cavity fibers. The reflected power map $P_R(\mathbf{r})$ which is recorded on a separate photodiode (see Fig 1d and SI) presents an interference pattern (between reflections on the nanowire and input fiber extremity) that strongly depends on the nanowire position $\mathbf{r} = \mathbf{r_0} + \delta\mathbf{r}$. The vibrations of its extremity $\delta\mathbf{r}(t)$ are dynamically encoded as photocurrent fluctuations $\delta P_R(t) = \delta\mathbf{r}(t)\cdot\boldsymbol{\nabla} P_R|_{\mathbf{r_0}}$ which allows to measure the nanowire vibrations $\delta r_\beta(t) = \delta\mathbf{r}(t)\cdot\mathbf{e}_\beta$ projected along the local measurement vector $\mathbf{e}_\beta \equiv \boldsymbol{\nabla} P_R/|\nabla P_R|$. Following the readout protocols described in ref. [1, 2, 5], this allows probing the nanowire thermal noise (see Fig. 3a grey curve) to determine its effective mass and verify its proper thermalisation, but also its response to an external force such as the one exerted by the intracavity light field. During those measurements, the cavity is locked on the pump laser, whose intensity is partially time-modulated using an acousto-optic modulator: $P_0+\delta P\cos\Omega t$ with an amplitude δP around a mean value P_0. The modulation frequency $\Omega/2\pi$ is swept across both eigenmode frequencies using a vectorial network analyser [1] and we record the optically induced driven displacement $\delta r_\beta[\Omega]$ as shown in Fig. 3a (black dots). The individual responses of each transverse mechanical mode are well distinguishable. The responses are well fitted in

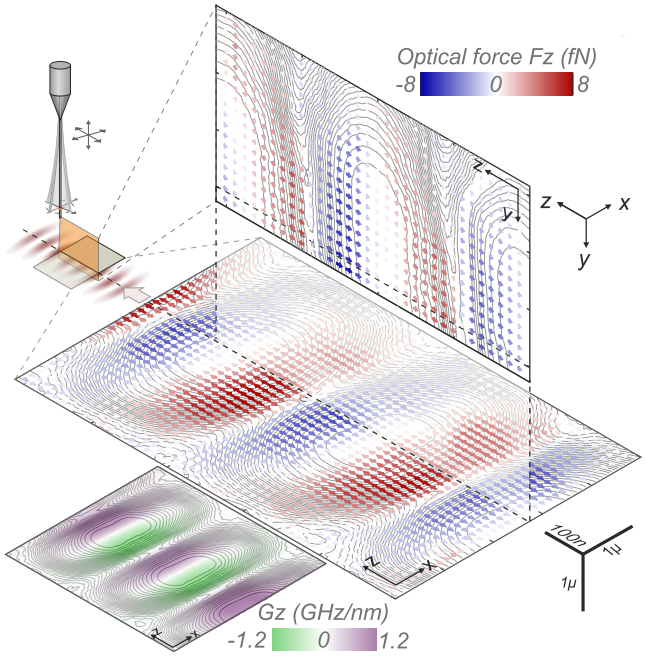

FIG. 4. **Nano-optomechanical mapping of the intracavity force field.** Horizontal (XZ) and vertical (YZ) maps of the intracavity force field (anisotropic length scales), measured for an injected power of $3\,\mu$W at 767 nm. The pump laser is injected along $\mathbf{e_z}$ and the dashed line represents the optical axis. The color code indicates the force component along the optical axis F_z. Inset: parametric coupling strength G_z derived from the correction of the cavity lock. The transmission iso-values are superimposed as gray lines to help visualizing the intracavity field structure.

amplitude and phase with the complex expression:

$$\delta r_\beta[\Omega] = \mathbf{e}_\beta \cdot \sum_{i=1,2} \chi_i[\Omega](\mathbf{e_i} \cdot \delta\mathbf{F})\mathbf{e_i}$$

where $\chi_i^{-1}[\Omega] \equiv M_{\rm eff}(\Omega_i^2 - \Omega^2 - i\Omega\Gamma)$, $(i = 1, 2)$ are the inverse mechanical susceptibilities of each eigenmodes. The measurement vector $\mathbf{e}_\beta$ is independently determined using the standard calibration protocols [1, 2]. The eigenmode orientations, frequencies, damping rates and effective masses are independently determined by fitting the Brownian motion spectra in absence of light modulation (see SI). Mode 1 is pointing at $+20°$ from the optical axis $\mathbf{e_z}$. As such, the only fitting parameter for the response measurement is the modulated force complex vector $\delta\mathbf{F}$ caused by the intensity modulation δP of the input light, which is modulating the mean intracavity photon number. Since the experiment is realized in the adiabatic cavity regime ($\Omega_{\rm m} \ll \kappa$), pure optical forces instantaneously follow (on mechanical timescales) the input light modulation, while photothermal forces [1] will be in quadrature (see SI). The amplitudes and orientations of the instantaneous optical force are reported in Fig. 3bc for increasing modulation depth of the intracavity photon number (produced by a modulation δP of the pump intensity). This allows to verify the linearity of the system response and to demonstrate its sensitivity to variations of the mean intracavity photon number smaller than unity. We measured a transduction efficiency of approx. 340 aN/photon for the optical force per intracavity photon number change (or a $2\,$fN/μW transduction efficiency related to the input optical power) at a given position of the nanowire extremity in the optical mode (indicated by $\odot$ in Fig. 2de, slightly besides a node). As expected, the optical force is aligned with the optical axis ($\mathbf{e_z}$), as reported in the inset of Fig. 3a. The magnitude of the measured force per intracavity photon is in good agreement with numerical simulations, see SI, predicting a 260 aN/photon transduction efficiency. At this position, the nanowire thermal noise limits its sensitivity to variations of the mean intracavity photon number at the level of $0.07\,\text{photon}/\sqrt{\text{Hz}}$ at 300 K.

Identical response measurements were subsequently realized at various locations along the optical axis. The resulting instantaneous optical force is reported in Fig. 3d. It was measured with a fixed modulation depth $\delta P/P_0 \approx 0.7$ for increasing average input powers P_0 (from 1 to $5\,\mu$W). The measured optical force is $\lambda/2$ periodic due to the standing wave periodicity. This type of force measurement inside a cavity is original. We found that it presents a repulsive character in the vicinity of the nodes of the intracavity field and on the contrary is found to be weakly attractive towards the antinodes of the intracavity field. Due to the multipolar character of the nanowire optical response, the interpretation of the force map can be delicate. However the phenomenology is well explained by theoretical modeling (see SI) and can be understood with the following qualitative argument, which also holds for membrane in middle experiments [38], for which the optical mode can be split into 2 sub-cavities located on each side of the oscillator. Regions of positive (resp. negative) dispersive shifts: $G_z > 0 (< 0)$ are then associated to situations where a larger amount of light is stored in the second (resp. first) sub-cavity, so that the total force is found negative (resp. positive). Also, the $\approx 30\%$ positive-negative asymmetry observed in the force extrema is connected to the laser pumping direction (along $\mathbf{e_z}$) and mirror asymmetries. The "saw tooth" pattern visible in the force variation along the optical axis is a consequence of the finesse reduction observed in the anti-nodes areas. There the force deviates from the oscillatory pattern that could be expected from the parametric measurement of G_z shown in Fig. 2.

The intracavity force field exerted on the nanowire $\mathbf{F}(z)$ presents some large spatial variations of $\partial_z F_z \approx 1.5 \times 10^{-7}\,$N/m for $5\,\mu$W input power in the vicinity of the intracavity nodes. They add up to the intrinsic nanowire stiffness, $k = M_{\rm eff}\Omega_{\rm m}^2 \approx 10^{-4}\,$N/m, and are responsible for frequency softening at the node locations. The measured frequency shifts are shown in

Fig. 3f, and are in good agreement with the ones deduced from the gradient of force measurements. This validates the force measurement protocol exposed above. We point out that those force measurements were realized using a largely frequency split nanowire ($\approx$ 20%), in order not to experience eigenmode rotations, which would have otherwise required a vectorial 2D readout of the nanowire displacements [2, 5].

Last, we pursued those measurements by mapping the intracavity 2D force field in 3D. Here we employed a faster measurement scheme in order not to suffer from spatial drifts, which should remain smaller than 10 nm over a few hours (corresponding to a 0.01° temperature stability). Instead of a full response measurement (Fig. 3a), we realized a simultaneous multi-frequency excitation drive at each position. A triplet of 3 optical drive tones was employed per mechanical mode, separated by 50 Hz, whose central frequency was locked onto the nanowire eigenfrequency with a soft peak tracking loop (see SI). This allows to simultaneously determine the local force, the mechanical frequencies and quality factors, while reducing the measurement time per point to 100 ms, 100 times faster than full response measurements. The measurement vector $\mathbf{e}_\beta$ was also locally recorded in real-time using a 2 tones (80-85 Hz) lock-in detection scheme (see SI).
The resulting XZ and YZ maps of the intracavity force field are shown in Fig. 4, superimposed on the transmission maps encoded as iso-values to help localizing the intracavity field structure. The color code shows the measured optical force projected along the optical axis (F_z), shown as colored arrows in the maps. Those measurements were realized using 400x400 pixels, lasting over 4 hours, and the signal processing routine described in the SI employed signal averaging up to 10 neighboring pixels, which correspond to a spatial resolution of 25 nm along the z axis. One can recognize the anti-trapping / trapping structures in the vicinity of the nodes /antinodes, and the vanishing of the optical force when the nanowire is extracted out of the intracavity mode volume, both transversally (x) and vertically (y). The parametric coupling map (G_z) is derived by calculating the gradient of the cavity lock correction signal map (see Fig. 2d, panel "cavity shift"), recorded during the same XZ measurement sequence. On each side of the antinodes, it is possible to identify locations of simultaneous large optical backaction and large parametric coupling strength. Those regions are clearly of great interest for future experiments in the single photon regime.
We note that operating with a quasi-frequency-degenerated nanowire and a full 2D readout scheme will allow future investigations of the possible non-reciprocal (non-conservative [5]) character of the intracavity force field and its impact on the nanowire dynamics.

Conclusion and prospectives– We have realized a dual characterization of the optomechanical interaction, via nanowire mediated scanning probe measurements of the intracavity field and mapping of the intracavity optomechanical force field using intracavity photon number modulations smaller than unity. This method permits to explore confined optical fields and provides a novel exploration tool, complementary to purely optical scanning probe measurements. The use of nanowires with sub-wavelength-sized diameters, permits to operate with ultrasensitive force sensors, but as a counterpart, generates a large optical scattering. However this does not prevent from largely entering the single photon regime at the condition to properly map the optomechanical interaction and to operate in the vicinity of the intracavity field nodes.
For consistency, all the experiments described in the manuscript were obtained with the same nanowire, but larger coupling strength, up to $g_0^z/2\pi = 2.6\,\mathrm{MHz} \approx 100 \times \Omega_\mathrm{m}/2\pi$, were reached with different nanowires, see SI. We note that the light-nanowire interaction can be further engineered and enhanced by exploiting higher order internal optical resonances (Mie) of the nanowire [8, 57], to take benefit from their multipolar optical response. Since we operate in the adiabatic regime, many perspectives of this work are to be found in quantum optics, where the large optomechanical interaction serves as a non-linear resource operating down to the single intracavity photon level. In particular it will allow investigating the deviations from the semi-classical approximation - where the fluctuations of the intracavity field have a similar impact as the mean field- and reaching a static bistability regime for less than one intracavity photon. To do so, one needs to reduce the oscillator thermal noise down to a level where the single photon recoil $\delta x^{(1)}$ becomes visible.
Operating with ultrasensitive kHz nanowires (see SI), such as the ones developed for operations at dilution temperatures [3], should permit to reach $\approx 7\,\mathrm{MHz}$ single photon coupling strength, while reducing their thermal noise spreading down to $\sqrt{n_T} \approx 500$ times their zero point fluctuations when thermalized at 20 mK (see SI). A single intracavity photon should then produce a static deformation of $\delta x^{(1)} \approx 8000\,\delta x_\mathrm{zpf}$ largely detectable on top of the nanowire residual rms thermal noise.
Furthermore, the exotic regime of single photon bistability should be achievable in our system since large single photon parametric cooperativities $\mathcal{C}^{(1)} \equiv 2g_0^2/\Omega_\mathrm{m}\kappa \approx 10$ can be achieved even with modest cavity linewidth (6 GHz). We also note that single photon cooperativities [1] as large as $g_0^2/\Gamma_\mathrm{m}\kappa \approx 4.2 \times 10^5$ are within reach.
Finally, one can estimate the possibility to detect the quantum fluctuations of the radiation pressure force noise in the single photon regime, which become observable if they exceed the Langevin force fluctuations. For a single mean intracavity photon, see SI, the ratio of the spectral densities of their respective force noise can be expressed [9] as $2C^{(1)}\,Q/n_\mathrm{T}$, which could reach approx. 30 at dilution temperatures.

Those considerations are thus strong incentives for pushing the developments towards dilution temperatures, to explore with mesoscopic oscillators the regime of single photon cavity optomechanics and possibly open the road towards scanning probe measurements of vacuum Casimir forces within confined optical resonators.

Acknowledgments– We warmly thank the PNEC group at ILM, T. Heldt for his assistance in the early phase of the experiment, S. Reynaud, F. Pistolesi, J. Estève, J.P. Poizat, G. Bachelier, J. Jarreau, C. Hoarau, E. Eyraud, A. Laurent and D. Lepoittevin. F.F. acknowledges funding from the LANEF (ANR-10-LABX-51-01). P.H. acknowledges funding from the European Union H2020 programme (Marie Sklodowska-Curie grant 754303). This project is supported by the French National Research Agency (JCJC-2016 CE09-2016-QCForce, SinPhoCOM, LANEF framework (ANR-10-LABX-51-01, project CryOptics and Investissements d'avenir program (ANR-15-IDEX-02, project CARTOF), and by the European Research Council under the EU's Horizon 2020 research and innovation programme, grant agreements No 671133 (EQUEMI project), 767579 (CARTOFF) and 820033 (AttoZepto).

[1] Aspelmeyer, M., Kippenberg, T. J. & Marquardt, F. Cavity optomechanics. *Rev. Mod. Phys.* **86**, 1391 (2014).
[2] Braginsky, V. B., Khalili, F. Y. & Thorne, K. S. *Quantum measurement* (Cambridge University Press, 1995).
[3] Caves, C. M. Quantum-mechanical radiation-pressure fluctuations in an interferometer. *Phys. Rev. Lett.* **45**, 75 (1980).
[4] Jaekel, M. T. & Reynaud, S. Quantum limits in interferometric measurements. *EPL* **13**, 301 (1990).
[5] Fabre, C. *et al.* Quantum-noise reduction using a cavity with a movable mirror. *Phys. Rev. A* **49**, 1337 (1994).
[6] Chan, J. *et al.* Laser cooling of a nanomechanical oscillator into its quantum ground state. *Nature* **478**, 89 (2011).
[7] Teufel, J. D. *et al.* Sideband cooling of micromechanical motion to the quantum ground state. *Nature* **475**, 359 (2011).
[8] Purdy, T. P., Peterson, R. W. & Regal, C. A. Observation of Radiation Pressure Shot Noise on a Macroscopic Object. *Science* **339**, 801 (2013).
[9] Peterson, R. W. *et al.* Laser Cooling of a Micromechanical Membrane to the Quantum Backaction Limit. *Phys. Rev. Lett.* **116**, 063601 (2016).
[10] Kampel, N. S. *et al.* Improving broadband displacement detection with quantum correlations. *Phys. Rev. X* **7**, 021008 (2017).
[11] Rossi, M., Mason, D., Chen, J., Tsaturyan, Y. & Schliesser, A. Measurement-based quantum control of mechanical motion. *Nature* **563**, 53 (2018).
[12] Weis, S. *et al.* Optomechanically induced transparency. *Science* **330**, 1520 (2010).
[13] Verhagen, E., Delglise, S., Weis, S., Schliesser, A. & Kippenberg, T. Quantum-coherent coupling of a mechanical oscillator to an optical cavity mode. *Nature* **482**, 63 (2012).
[14] Palomaki, T. a., Teufel, J. D., Simmonds, R. W. & Lehnert, K. W. Entangling mechanical motion with microwave fields. *Science* **342**, 710 (2013).
[15] Lecocq, F., Clark, J. B., Simmonds, R. W., Aumentado, J. & Teufel, J. D. Quantum nondemolition measurement of a nonclassical state of a massive object. *Phys. Rev. X* **5**, 041037 (2015).
[16] Riedinger, R. *et al.* Non-classical correlations between single photons and phonons from a mechanical oscillator. *Nature* **530**, 313 (2016).
[17] Sudhir, V. *et al.* Appearance and disappearance of quantum correlations in measurement-based feedback control of a mechanical oscillator. *Phys. Rev. X* **7**, 011001 (2017).
[18] Pirkkalainen, J.-M., Damskägg, E., Brandt, M., Massel, F. & Sillanpää, M. A. Squeezing of Quantum Noise of Motion in a Micromechanical Resonator. *Phys. Rev. Lett.* **115**, 243601 (2015).
[19] Peterson, G. A. *et al.* Ultrastrong parametric coupling between a superconducting cavity and a mechanical resonator. *Phys. Rev. Lett.* **123**, 247701 (2019).
[20] Reynaud, S., Fabre, C., Giacobino, E. & Heidmann, A. Photon noise reduction by passive optical bistable systems. *Phys. Rev. A* **40**, 1440 (1989).
[21] Bose, S., Jacobs, K. & Knight, P. L. Preparation of nonclassical states in cavities with a moving mirror. *Phys. Rev. A* **56**, 4175 (1997).
[22] Mancini, S., Man'ko, V. & Tombesi, P. Ponderomotive control of quantum macroscopic coherence. *Phys. Rev. A* **55**, 3042 (1997).
[23] Ludwig, M., Kubala, B. & Marquardt, F. The optomechanical instability in the quantum regime. *New J. Phys.* **10**, 095013 (2008).
[24] Rabl, P. Photon blockade effect in optomechanical systems. *Phys. Rev. Lett.* **107**, 063601 (2011).
[25] Nunnenkamp, A., Borkje, K. & Girvin, S. M. Single-photon optomechanics. *Phys. Rev. Lett.* **107**, 063602 (2011).
[26] Nunnenkamp, A., Børkje, K. & Girvin, S. M. Cooling in the single-photon strong-coupling regime of cavity optomechanics. *Phys. Rev. A* **85**, 051803(R) (2012).
[27] He, B. Quantum optomechanics beyond linearization. *Phys. Rev. A* **85**, 063820 (2012).
[28] Hong, T., Yang, H., Miao, H. & Chen, Y. Open quantum dynamics of single-photon optomechanical devices. *Phys. Rev. A* **88**, 023812 (2013).
[29] Nation, P. D. Nonclassical mechanical states in an optomechanical micromaser analog. *Phys. Rev. A* **88**, 053828 (2013).
[30] Rimberg, A. J., Blencowe, M. P., Armour, A. D. & Nation, P. D. A cavity-Cooper pair transistor scheme for investigating quantum optomechanics in the ultra-strong coupling regime. *New J. Phys.* **16**, 055008 (2014).
[31] Frisk Kockum, A., Miranowicz, A., De Liberato, S., Savasta, S. & Nori, F. Ultrastrong coupling between light and matter. *Nature Reviews Physics* **1**, 19 (2019).
[32] Forn-Díaz, P., Lamata, L., Rico, E., Kono, J. & Solano,

E. Ultrastrong coupling regimes of light-matter interaction. *Rev. Mod. Phys.* **91**, 025005 (2019).

[33] Murch, K. W., Moore, K. L., Gupta, S. & Stamper-kurn, D. Observation of quantum-measurement backaction with an ultracold atomic gas. *Nat. Phys.* **4**, 561 (2008).

[34] Brennecke, F., Ritter, S., Donner, T. & Esslinger, T. Cavity optomechanics with a bose-einstein condensate. *Science* **322**, 235 (2008).

[35] Leijssen, R. & Verhagen, E. Strong optomechanical interactions in a sliced photonic crystal nanobeam. *Sci. Rep.* **5**, 15974 (2015).

[36] Leijssen, R., La Gala, G. R., Freisem, L., Muhonen, J. T. & Verhagen, E. Nonlinear cavity optomechanics with nanomechanical thermal fluctuation. *Nat. Commun.* **8**, 16024 (2017).

[37] Reinhardt, C., Müller, T., Bourassa, A. & Sankey, J. C. Ultralow-noise sin trampoline resonators for sensing and optomechanics. *Phys. Rev. X* **6**, 021001 (2016).

[38] Thompson, J. D. *et al.* Strong dispersive coupling of a high-finesse cavity to a micromechanical membrane. *Nature* **452**, 72 (2008).

[39] Favero, I. *et al.* Fluctuating nanomechanical system in a high finesse optical microcavity. *Opt. Express* **17**, 12813 (2009).

[40] Anetsberger, G. *et al.* Near-field cavity optomechanics with nanomechanical oscillators. *Nat. Phys.* **5**, 909 (2009).

[41] Sankey, J. C., Yang, C., Zwickl, B. M., Jayich, A. M. & Harris, J. G. E. Strong and tunable nonlinear optomechanical coupling in a low-loss system. *Nat. Phys.* **6**, 707 (2010).

[42] Stapfner, S. *et al.* Cavity-enhanced optical detection of carbon nanotube Brownian motion. *Appl. Phys. Lett.* **102**, 151910 (2013).

[43] Favero, I., Sankey, J. & Weig, E. M. *Mechanical Resonators in the Middle of an Optical Cavity*, 83 (Springer Berlin Heidelberg, 2014).

[44] Kiesel, N. *et al.* Cavity cooling of an optically levitated nanoparticle. *PNAS* **110**, 14180 (2013).

[45] Jöckel, A. *et al.* Sympathetic cooling of a membrane oscillator in a hybrid mechanicalatomic system. *Nat. Nanotechnol.* **10**, 55 (2015).

[46] Wilson, D. J. *et al.* Measurement-based control of a mechanical oscillator at its thermal decoherence rate. *Nature* **524**, 325 (2015).

[47] Arcizet, O. *et al.* A single nitrogen-vacancy defect coupled to a nanomechanical oscillator. *Nat. Phys.* **7**, 879 (2011).

[48] Gloppe, A. *et al.* Bidimensional nano-optomechanics and topological backaction in a non-conservative radiation force field. *Nat. Nanotechnol.* **9**, 920 (2014).

[49] Pigeau, B. *et al.* Observation of a phononic mollow triplet in a multimode hybrid spin-nanomechanical system. *Nat. Commun.* **6**, 8603 (2015).

[50] Mercier de Lépinay, L. *et al.* A universal and ultrasensitive vectorial nanomechanical sensor for imaging 2D force field. *Nat. Nanotechnol.* **12**, 156 (2016).

[51] Rossi, N. *et al.* Vectorial scanning force microscopy using a nanowire sensor. *Nat. Nanotechnol.* **12**, 150 (2017).

[52] Mercier de Lépinay, L., Pigeau, B., Besga, B. & Arcizet, O. Eigenmode orthogonality breaking and anomalous dynamics in multimode nano-optomechanical systems under non-reciprocal coupling. *Nat. Commun.* **9**, 1401 (2018).

[53] Colombe, Y. *et al.* Strong atom - field coupling for Bose - Einstein condensates in an optical cavity on a chip. *Nature* **450**, 272 (2007).

[54] Hunger, D. *et al.* A fiber Fabry-Perot cavity with high finesse. *New J. Phys.* **12**, 065038 (2010).

[55] Mader, M., Reichel, J., Hänsch, T. W. & Hunger, D. A scanning cavity microscope. *Nat Commun* **6**, 7249 (2015).

[56] Ferri, F., Garcia, S., Baghdad, M., Reichel, J. & Long, R. Mapping standing-wave cavity modes with a commercial scanning near-field microscope tip. *Rev. Sci. Instrum.* **91**, 033104 (2020).

[57] Bohren, C. F. & Huffman, D. *Absorption and Scattering of Light by Small Particles* (WileyVCH, Berlin, 1983).

[58] Reigue, A. *et al.*. Cavity nano-ptomechanics with suspended nanowires: modelisation and novel phenomenology. *in preparation* (2020).

[59] Hunger, D., Deutsch, C., Barbour, R. J., Warburton, R. J. & Reichel, J. Laser micro-fabrication of concave, low-roughness features in silica. *AIP Advances* **2**, 012119 (2012).

[60] Fogliano, F. *et al.* Ultrasensitive nano-optomechanical force sensor at dilution temperatures. *Arxiv:2009.02912* (2020).

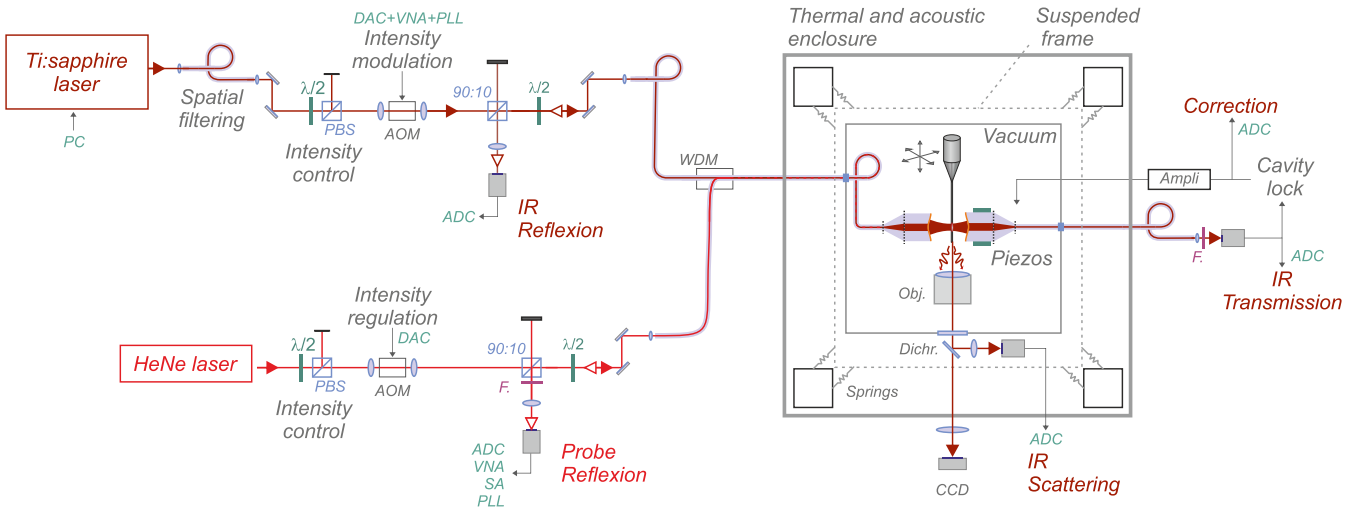

FIG. 5. **Detailed experimental setup.** F.: filters, ADC/DAC: inputs/outputs of the acquisition card, Dichr.: dichroic filter, WDM: wavelength combiner, IR: infrared The core experiment is realized in a vacuum chamber, mounted on a suspended plate, which hosts the lateral IR scatter detector. The experiment is mounted in a multi-layer acoustic and thermal isolation box.

Appendix A: The experiment

1. Description of the experiment

The infrared laser source is a tunable and low noise Ti:sapphire laser, with sub-100 kHz linewidth. It is employed between 760 and 820 nm depending on the optical finesse needed. The later can thus be tuned between 200 and 45 000. Its output is spatially filtered using a monomode fiber, its intensity is controlled, with an acousto-optic modulator. A non-polarizing 90:10 beam splitter is employed to collect the light reflected from the cavity, and the injection polarization is controlled by a $\lambda/2$ wave plate. The experiment is operated in a vacuum chamber to eliminate acoustic damping. A pressure below 10^{-2} mbar can be statically maintained over several days, which is sufficient to realize the long-term acquisition needed. The vacuum chamber is suspended above an optical table using 4 bungee cables to reduce acoustic vibrations, and inserted in a thermal and acoustic foam insulation chamber to improve its temperature stability and further reduce acoustic vibrations.

The injection fiber is directly attached to a breadboard in the vacuum chamber, while the transmission fiber is mounted on a motorized XYZ stage and on a gimbal mount to adjust the fiber lateral position and its orientation with respect to the injection fiber. Both fibers are supported by annular piezo elements which are used to control and dither the cavity length. A coarse piezo stack enables an $\approx 1.1\,\mu$m scan range, which is sufficient to cover several free spectral range of the cavity. A rapid piezo element is employed to dither the cavity length by approx. 0.1 nm at 250 kHz, in order to provide the error signal for the cavity lock.

The cavity transmission is detected outside of the optical chamber, while a 20x/0.4NA microscope objective, positioned perpendicularly to the optical axis serves to collect the light scattered by the nanowire. The later is focused on a photodiode positioned on the vacuum chamber support.

The nanowire is mounted on a XYZ piezo stage, providing travel ranges of $30 \times 30 \times 10\,\mu$m along the XYZ axes. It is supported by a motorized XYZ stage used for coarse positioning. The nanowire support can be rotated in order to align the nanowire with the XY plane, which permits inserting the nanowire in small mode volumes optical modes. In practice, we first optimize the second fiber angles in absence of nanowire, then open the cavity up to a length of $200\,\mu$m, insert the nanowire in the mode volume area and then progressively close the cavity while continuously optimizing the angles and lateral position of the second fiber. All those pre-alignments steps can be realized by monitoring the transmission signals.

Since the optical shifts induced by the nanowire are extremely large (400 GHz), and are significantly larger than the mode-hope free scan range of the laser (30 GHz), we chose to lock the cavity length on the laser frequency. The error signal and the feedback gains are produced and processed by a FPGA card based on the PyRPL code developments. We dither the cavity length using the rapid piezo element, and feedback on the piezo stack at low frequencies (up to ≈ 200 Hz), while a second loop employs the fast piezo (up to few kHz). The

lock is rather robust and agile, and allows to maintain the cavity resonant for days, even in presence of the nanowire, which can largely reduce the transmission level (down to 5%). The lock bandwidth is intentionally limited in order not to compensate for the dynamical parametric cavity shifts induced by the nanowire motion. As such mechanical motion remains visible in the lock error signal, which provides a complementary readout channel for mechanical vibrations. Depending on the experiments envisioned, one can also increase the lock bandwidth beyond the nanowire mechanical resonance (the first internal resonance of the fast piezo ring element is around 300 kHz) in order to compensate for position fluctuations so that the cavity remains dynamically locked.

The mirror curvatures are measured during the microfabrication phase. The determination of the cavity length is realized by measuring the spectral distance between 2 optical resonances using the large tunability of the pump lasers, and by measuring of the spectral arrangement of the transverse mechanical modes. Measurements were realized with 2 sets of almost identical fibers, with radii of curvature of 29 μm and 60 μm. All the measurements shown in the article are obtained with the first set of fibers. We have also investigated the parametric coupling and the force field structure of other transverse modes, as well as cross-couplings induced by the nanowire. The nanowires allows a clear identification of the nature intracavity modes. Also, we employed the nanowire in order to carefully align the intracavity mode: depending on the fiber positions and orientations, the optical mode can be found twisted with respect to the fiber axes.

In order to probe the nanowire vibrations independently from the cavity mode, we made use of a visible 633 nm laser, which is co-injected in the cavity fibers using fibered wavelength dividing modules (WDM) and whose reflection is collected using a 90:10 non-polarizing beam splitter. The partial reflections on the fiber extremity (falling outside of the reflectivity window of the mirror coatings) and the one coming from the nanowire interfere and are responsible for a spatial XZ structuration of the red reflection image. When the nanowire oscillates, it dynamically modulates the reflected signal, and the principles of projective readout [1, 2] can be employed similarly (see Fig.12). The experiment is interfaced by a software which controls the nanowire position in 3D, the cavity length, and records the different optical signals, as well as demodulation signals produced by the PLL (see below). The nanowire vibrations are recorded using signal and network analyzers, and a dual PLL which is employed for the multi-frequency response measurements (see below).

The experiment is pre-aligned at room pressure, by taking a special care on the fiber tilt angles in order to produce an optical cavity mode presenting a good mode matching to the fibers, and oriented perpendicularly to the nanowire axis (and if possible along the Z axis of the piezo stage moving the nanowire). Before pumping the chamber, we retract the fibers by approx. 100 μm so that the pump vibrations do not make the nanowire stick the fibers end faces, and the system is re- aligned at low pressure. It was important to stop the side illumination during the fine alignment phase, in order to limit spatial drifts in the experiment. At some occasions, we observed electrostatic charging in the system, which was causing the nanowire sticking to the fibers extremities. In general after a few hours, the effect disappeared. The fiber sides are metal coated to sustain the optical coating, which also serves to partly shield the fiber extremities from the electric stray field produced by the closest by piezo elements (0-100 V, at 1 cm distance). Their impact on the nanowire dynamics - the nanowire is attracted towards regions of large electric field - could occasionally be detected for very small cavities, as a residual force field gradient, but are most of the time far smaller than the optical forces involved in the experiment.

2. Internal Mie resonances

Fig. 6 illustrates the role of internal Mie resonances on the light-nanowire interaction.

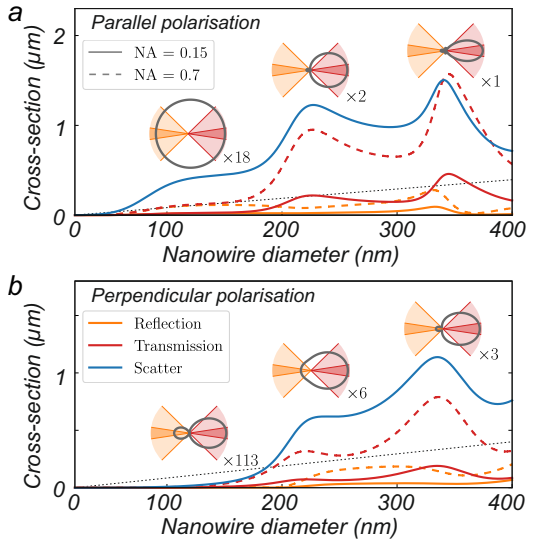

FIG. 6. **Nanowire multipolar optical response: Mie resonances.** Scattering cross sections for infinite SiC cylinders under plane wave illuminations incoming from the left hand side, for increasing nanowire diameters. The reflection, transmission and scatter components are integrated in the backward, forward and lateral angular segments respectively. The total linear cross section can largely excess the nanowire diameter (indicated by a black line) and varies rapidly with the nanowire diameter due to the Mie resonances. The nanowire optical response can be assimilated to a dipole for diameters smaller than approx. 100 nm, while its multipolar character must be taken into account for the nanowires employed in that work (130 and 160 nm in diameter).

NW	L(μm)	d(nm)	$\Omega_m/2\pi$(kHz)	Q	M_{eff}(pg)	dF_{min}(aN/Hz$^{1/2}$)	$g_0^z/2\pi$(MHz)	g_0/Ω_m
NW1 (article)	70	130	$50-60$	2000	0.7	$25(300K)$	1.3	25
NW2 (SI Fig.8)	90	160	$27.2-27.6$	2700	2	$30(300K)$	2.6	96
NW3	400	160	1.6	100 000	6.6	0.02(20 mK)	7	4300

TABLE I. **Nanowires discussed in this work** NW1 and NW2 were tested at room temperature in the cavity. NW3 is an estimation based on the typical nanowires investigated at dilution temperatures [3] with a 10 μm cavity length.

3. Nanowire samples

Several nanowires were employed in this project, see Table I. For a given cavity mode, the parametric coupling strength ($\vec{G}$) only depends on the nanowire diameter. We employed different nanowires with diameters ranging from 100 to 250 nm. All the results presented in the article are realized with a 130 nm diameter nanowire, while the largest coupling strengths could be achieved using a 160 nm diameter nanowire as shown in Fig.8.
The NW3 line represents an extrapolation at dilution temperature based on recent results obtained [3] where we could detect the thermal noise of SiC nanowires thermalized down to 20 mK using a single path optical readout. Using a modest 6 GHz cavity linewidth (2000 finesse), this nanowire should permit to reach a single photon parametric cooperativity of $\mathcal{C}^{(1)} \equiv 2g_0^2/\Omega_m\kappa = 9.5$ and a single photon cooperativity of $g_0^2/\Gamma_m\kappa = 426\,000$.

4. Aspect ratio of the scanning images

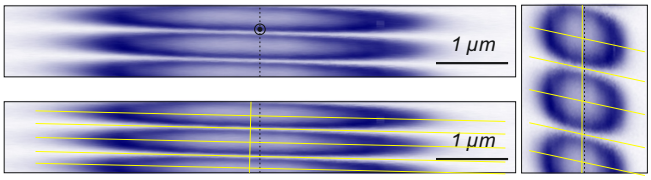

FIG. 7. **Aspect ratio of the scanning images.** Representations of Fig 2d scatter channel, shown with their true aspect ratio on the left. In the lower left plot, a tilted perpendicular grid has been added. The tilt angle is $-1.7°$. The black circle represents the dimensions of a 150 nm diameter nanowire, given for comparison. The image axes (XZ) are the ones set by the XYZ piezo stage moving the nanowire. Right: the same image shown with the squeezed aspect ratio employed in Fig. 2 is on the right. The deformation of the perpendicular grid is an artefact of the aspect ratio chosen.

5. Optomechanical coupling to nanowire NW2

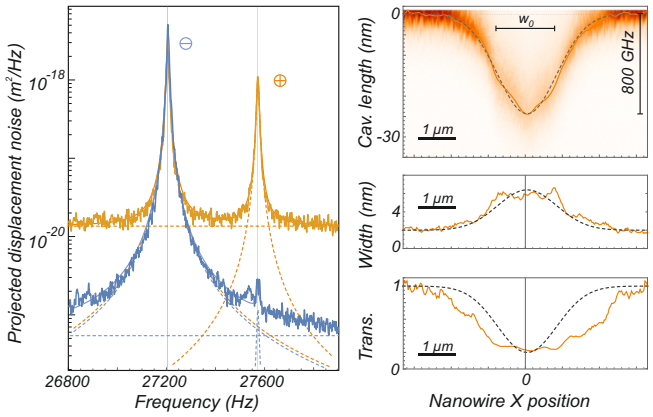

FIG. 8. **Coupling strength with a 160-nm diameter nanowire (NW 2).** Left: thermal noise at 300 K of a 160-nm diameter nanowire, measured along two measurement channels [2]. It presents an effective mass of 2×10^{-15} kg, oscillates at 27200 and 27580 Hz, with a $\Gamma_m/2\pi = 10$ Hz damping rate. In this measurement, the lower eigenmode orientation was oriented perpendicular to the optical axis, to be ideally read by the differential channel $\ominus$. It conveys a 30 aN/$\sqrt{\text{Hz}}$ force sensitivity, with thermal noise spreading over $\Delta x_{th} = 7.8$ nm(64pm) at 300 K (20 mK) and zero point fluctuations spreading over $\delta x_{zpf} = 0.4$ pm. Right: cavity resonant length shifts measured at 767 nm, while scanning the nanowire transversally (X axis) across the cavity mode, through an antinode (fitted optical waist of $w_0 = 1.6\,\mu$m). The maximum parametric shifts amounts to a cavity length change of -24.7 nm (total length 12 μm), corresponding to an equivalent +800 GHz resonance frequency increase. The corresponding maximum slopes are $G_x/2\pi = 0.6$ GHz/nm and $G_z/2\pi = 6.5$ GHz/nm, and lead to a single photon coupling strength of $\mathbf{g_0} = (0.24, 2.6)$ MHz, which represents a maximum ultrastrong coupling ratio g_0/Ω_m of approx. 100. The dynamical rms broadening of the cavity resonance is of approx.$G_z\Delta x_{th} \approx 2\pi\,50$ GHz in frequency, or 1.6 nm in effective resonance width, which is slightly smaller than the 4 nm line broadening observed [4].

Appendix B: Force measurements

The optical force measurements were realized using a pump-probe technique. The nanowires vibrations are readout using the red probe beam, while the optical force is intensity modulated around a mean static value.

1. Optical readout of the nanowire vibrations

Due to the interference between the probe light reflected from the input cavity mirror and the one reflected from the nanowire and collected back into the fiber, the reflected intensity ($P_R(\mathbf{r})$) presents spatial variations that depend on the nanowire position. When the nanowire oscillates with a vectorial deflection $\delta\mathbf{r}$ around its rest position $\mathbf{r_0}$, it generates a modulated output voltage of $P_R(\mathbf{r_0}+\delta\mathbf{r}(t)) \approx P_R(\mathbf{r_0}) + \delta\mathbf{r}(t)\cdot\boldsymbol{\nabla}P_R|_{\mathbf{r_0}}$. The fluctuations of the photodiode output permits to realize a projective readout of the nanowire motion $\delta\mathbf{r}$ along a measurement vector $\mathbf{e}_\beta$, which is defined as $\mathbf{e}_\beta \equiv \boldsymbol{\nabla}P_R|_{\mathbf{r_0}} / |\boldsymbol{\nabla}P_R|_{\mathbf{r_0}}|$. The latter is determined by measuring the local gradient of the reflected power map. To do so, we employ two methods: a static and dynamical one. In the static mode, we record the reflected signal for different positions of the nanowire, placed on a 20 nm grid around the measurement position. We then compute the local tangent plane to the surface $P_R(\mathbf{r})$, from which we extract the local gradient [1, 2]. In the dynamical mode, which permits a faster evaluation of the measurement angle, we dynamically modulate the nanowire rest position in the XZ planes at 2 different frequencies (80 and 85 Hz) and demodulate the reflected signal. The amplitude and phase of both signals are then used to determine the local slope and orientations of the gradient along the 2 axes. Fig. 12 shows a map of the measurement vectors measured during the multi-frequency XZ map shown in Fig. 4 of the article. The oscillation amplitudes employed for the dynamical calibration of the measurement vectors are of a few nanometers. Those calibration tones are interrupted during the measurement phase, in order not to additionally shake the nanowire during the measurement process.

The fluctuations of the photodiode output are recorded on spectrum and network analyzers, as shown in Fig.8 and the Fig.3 of the manuscript. In absence of external drive, we can record the thermal noise of the nanowire, which permits determining the effective mass $M_{\rm eff}$, eigenfrequencies Ω_1, Ω_2, damping rate Γ_m and eigenmode orientations $\mathbf{e_1}, \mathbf{e_2}$ of the 2 fundamental transverse eigenmodes [2]. In those experiments, we only rely on a single measurement channel, meaning that we have to assume that the eigenmode orthogonality is preserved [2, 5]. In practice we have intentionally employed a nanowire presenting a large frequency splitting (50-60 kHz) to reduce the eigenmode rotation caused by the force field. After having mapped the force field, we can verify that its spatial variations do not generate appreciable eigenmode rotations.

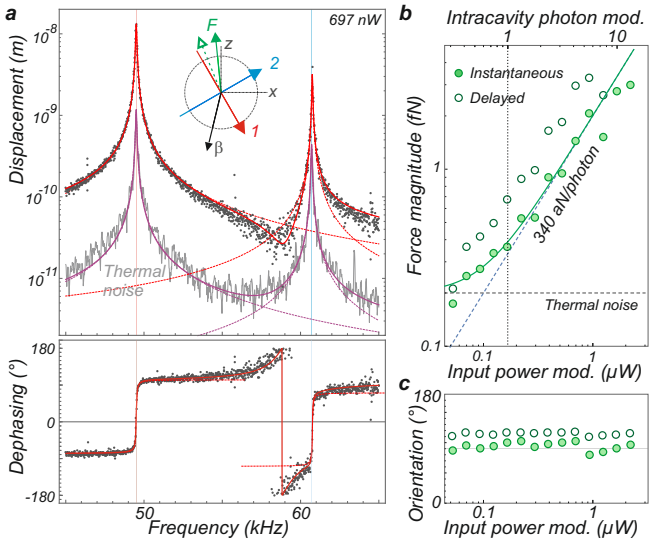

FIG. 9. **Delayed photothermal forces.** Inclusion of delayed optical forces, of photothermal origin, in Fig. 3. The open symbols represent the magnitudes and orientations of the delayed force vectors, at the measurement position, for increasing modulation depth. The full symbols represent the instantaneous optical forces.

2. Nanowire dynamics, thermal noise and response measurements

The nanowire dynamics can be written in the Fourier domain:

$$\delta\mathbf{r}[\Omega] = \boldsymbol{\chi}[\Omega]\cdot(\delta\mathbf{F}_{\rm th} + \mathbf{F_{opt}}[\Omega]) \tag{B1}$$

where the 2D mechanical susceptibility is given by:

$$\boldsymbol{\chi}^{-1}[\Omega] \equiv M_{\rm eff}\begin{pmatrix} \Omega_1^2 - \Omega^2 - i\Omega\Gamma_{\rm m} & 0 \\ 0 & \Omega_2^2 - \Omega^2 - i\Omega\Gamma_{\rm m}\end{pmatrix} \tag{B2}$$

in the $(\mathbf{e_1}, \mathbf{e_2})$ base. The Langevin force vector $\delta\mathbf{F}_{\rm th} = (\delta F_1^{\rm th}, \delta F_2^{\rm th})$ is composed of 2 Langevin forces, independently driving the nanowire along the eigenmode orientations. They present a zero mean value and a white noise spectral density given by the fluctuation dissipation theorem of $S_F \equiv 2M_{\rm eff}\Gamma_{\rm m}k_BT$. The optical force vector is given by $F_{\rm opt}(t)$ and depends on the injected IR light intensity $P(t)$. It can be time modulated at a frequency $\Omega/2\pi$ with an amplitude δP around a mean value P_0 using an acousto optic modulator $P(t) = P_0 + \delta P\cos(\Omega t)$. In that case, the optical force will present a static component (which can displace the nanowire rest position, but

can be neglected in practice) and an oscillating counterpart $\delta\mathbf{F}_{\rm opt}\cos(\mathbf{\Omega t}+\varphi)$. In case of a pure optical force and in the adiabatic cavity limit ($\Omega_{\rm m} \ll \kappa$) where we operate, the intracavity force instantaneously follows on mechanical time-scales the time fluctuations of the input intensity ($\varphi = 0$). In case of thermal-optical forces, the establishment of the force may be delayed. Previous analysis [1] have shown that the thermal dephasing is of 90 degrees at room temperature (thermal cutoff around 1 kHz for the nanowires employed in that work). As such the Fourier component of the time modulated optical force vector can be generally written:

$$\delta\mathbf{F}_{\rm opt}[\Omega] = \delta F \mathbf{e_F} + i\ \delta\tilde{F}\mathbf{e}_{\tilde{\mathbf{F}}}. \quad \text{(B3)}$$

The projective readout permits to record $\delta r_\beta[\Omega]$ given by:

$$\delta r_\beta[\Omega] = \mathbf{e}_\beta \cdot \delta\mathbf{r}[\Omega] = \mathbf{e}_\beta \cdot \boldsymbol{\chi}[\Omega] \cdot (\delta\mathbf{F}_{\rm th} + \mathbf{F_{opt}}[\Omega]) \quad \text{(B4)}$$

In absence of optical modulation, one can record the thermal noise of the nanowire, whose spectral density is given by:

$$S_{\delta r_\beta}[\Omega] = \sum_{i=1,2} (\mathbf{e}_\beta \cdot \mathbf{e_i})^2 \frac{S_F}{M_{\rm eff}^2\left((\Omega_i^2-\Omega^2)^2+\Omega^2\Gamma_{\rm m}^2\right)} \quad \text{(B5)}$$

This expression is used to adjust the thermal noise spectra, and allows to determine the mechanical parameters of the nanowire (frequencies, damping rates, effective mass) and the effective temperature of the modes. One can verify their proper thermalization, at 300K, by varying the optical readout power. In presence of the IR cavity light field, the mechanical properties can evolve due to the spatial gradients of the optical forces. If one uses a single measurement channel, one needs to assume that the eigenmodes remains orthogonal to correctly evaluate its response to an external force, this is why we employed a largely frequency split nanowire, which is protected against eigenmode rotations [5]. In practice, we realized optical measurements mainly on the reflected red channel, but we complemented it using the scatter IR light and the IR transmission channel.

In presence of an external optical drive, we employed a network analyzer to measure the steady state trajectory of the nanowire, while sweeping the drive frequency across both eigenmodes. To correctly estimate the overall delays in the VNA measurement, one can simply remove the IR filter in front of the detector collecting the probe laser reflexion (the WDM is not perfectly canceling the IR signal). This allows to compensate for the electronic delays in the detection channel and in the drive channel. In that situation, we then directly record the magnitude of $\delta r_\beta[\Omega]$ and its dephasing with respect to the intensity modulation. The response data are thus adjusted by :

$$\delta r_\beta[\Omega] = \sum_{i=1,2} \frac{(\mathbf{e}_\beta \cdot \mathbf{e_i})(\delta\mathbf{F}[\Omega]\cdot\mathbf{e_i})}{M_{\rm eff}\left(\Omega_i^2-\Omega^2-i\Omega\Gamma_{\rm m}\right)} \quad \text{(B6)}$$

All the mechanical and readout parameters are already independently determined, so that the only fitting parameter is the complex drive vector $\delta\mathbf{F}[\Omega]$, which possesses 4 degrees of freedom (real and imaginary parts of both spatial components). In practice, we employ the expression (B3), so that the fitting parameters are the magnitudes $(\delta F, \delta\tilde{F})$ and orientations $(\mathbf{e_F}, \mathbf{e}_{\tilde{\mathbf{F}}})$ of the instantaneous and delayed force components. They are shown in Fig.9. The gradients of the delayed photothermal forces modify the nanowire damping matrix, so that the nanowire mechanical damping rates must be determined in each position. The end of the article is only focused on the instantaneous optical force, the one of interest in cavity optomechanics, whose spatial gradients can generate mechanical frequency shifts and eigenmode rotations, as analysed in Fig. 3f.

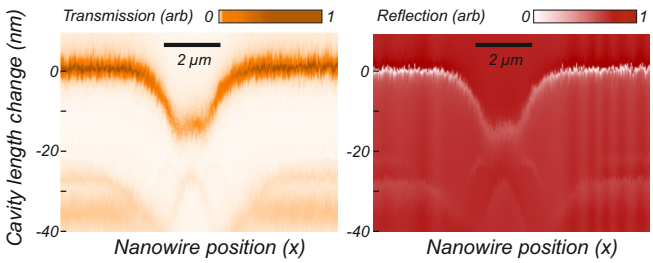

FIG. 10. **Nanowire based scanning probe exploration of the intracavity field and higher order transverse modes.** Cavity IR transmission and reflection stacks measured while scanning its total length with the slow piezo and moving the nanowire across the optical mode (x axis). For this cavity configuration, in addition to the $\rm TEM_{00}$ mode (top), higher orders modes are also visible (bottom) and cross-couplings can be induced by the nanowire diffusion.

3. Higher order optical cavity modes

It is possible to investigate the optomechanical coupling between the nanowire and higher order transverse modes of the cavity, whose transverse structure can be identified by scanning the nanowire within the cavity mode (see Fig.10). The optomechanical force field experienced when pumping the $\rm TEM_{12}$ mode is shown in Fig. 11.

4. Multi-frequency response measurements

The above procedure based on full response measurements requires to stay at least a duration of $1/\Gamma_{\rm m}$ per frequency point (100 ms) so that the full acquisition

requires at least 20-30 s per point before fitting the response data that allows to determine the local optical force vector. It is possible to largely accelerate the measurement duration by exploiting the large linearity of the apparatus and driving the nanowire simultaneously with several (6) frequencies and demodulating the different driven trajectories. In order to simultaneously determine the eigenmode frequencies and damping rates and to compensate for possible variations due to force field gradients or thermal drifts, we choose to employ 3 tones per mechanical mode, at frequencies $\Omega_i^{0,\pm1}$ separated by 50 Hz which is comparable to the eigenmode linewidth. The central frequency Ω_i^0 is maintained close to the mechanical resonance using a soft tracking via a peak detection mode on a fast spectrum analyzer. Those measurements are realized using a multi-frequency synchronous detector (Zurich Instrument HF2LI) and permit to reduce the measurement duration to 100 ms per point, at least 100 times faster than the above response measurements.

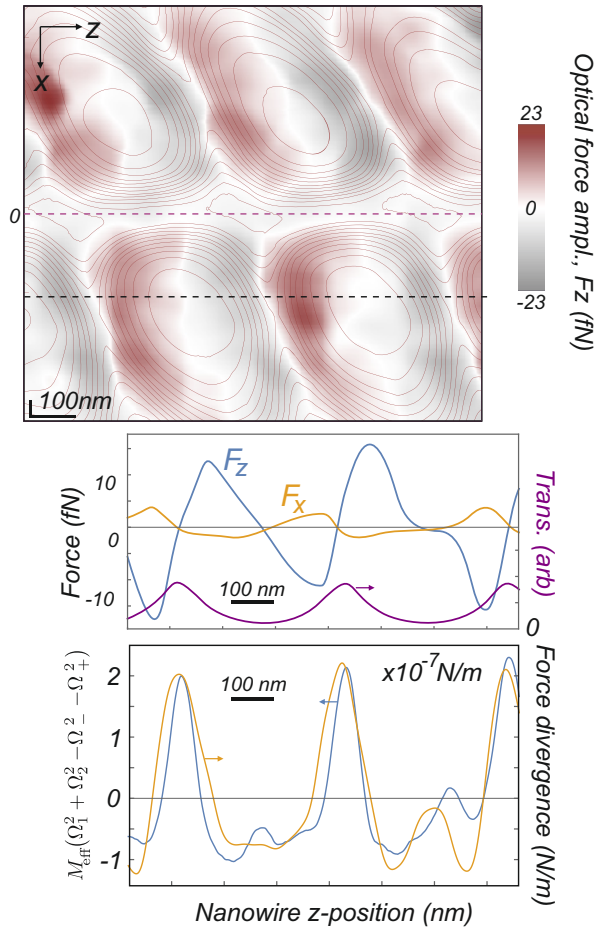

FIG. 11. **Optomechanical force field obtained with a TEM$_{12}$ mode.** Top: multi-frequency force field measurement realized when locking the cavity on a higher order transverse mode. The map is interpolated from a 400x400 measurement grid. The gray lines are iso-transmission lines. Middle: cuts along the z direction (dashed line in the map, on the side of the optical axis) of the force components. Bottom: force divergence deduced from mechanical frequency shifts (blue) and spatial derivation of the force map (orange), evaluated along the same cut in the map.

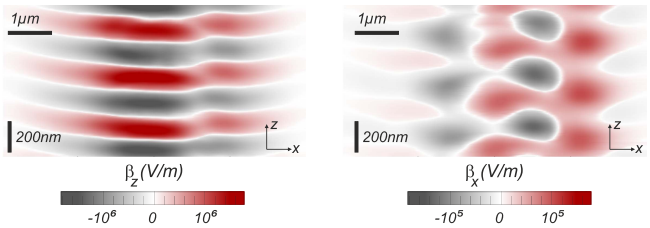

FIG. 12. **Maps of the measurement vectors.** XZ maps of the measurement vectors (β_z, β_x) obtained with the spatial interference measured on the red probe laser reflexion photodiode signal $P_R(\mathbf{r_0})$. Measurement vectors defined as $\boldsymbol{\beta} \equiv \boldsymbol{\nabla} P_R$ are measured dynamically, by modulating the piezo stage supporting the nanowire with constant tones at 80 and 85 Hz along the x and z axes (approx. 5 nm of amplitude) and demodulating the photodiode output signal ($1-10\,\mu$W of 633 nm probe laser are typically employed). Those measurements are acquired simultaneously during the multi-frequency response maps shown in Fig. 4 of the article, on a 400x400 pixel map, with 100 ms acquisition time per point. The z-periodicity observed corresponds to half the probe laser wavelength (633 nm). In most positions, the measurement vectors $\mathbf{e}_\beta = \boldsymbol{\beta}/|\boldsymbol{\beta}|$ are almost aligned with the optical axis $\mathbf{e_z}$.

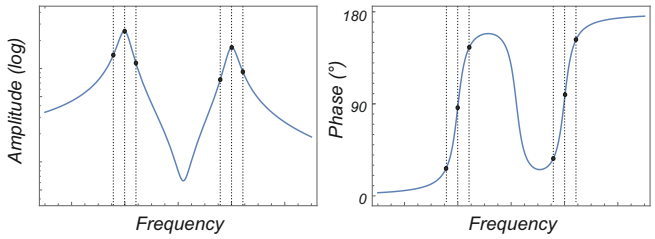

FIG. 13. **Principle of multi-frequency response** The nanowire is simultaneously driven by the intracavity field at 6 different frequencies, in order to accelerate the measurement time of the local force vector. 3 tones are driving each eigenmode, the central tone of which is locked on the eigenmode resonance, while the 2 sidebands are separated by 50 Hz, which is comparable to the eigenmode linewidth. Recording the amplitudes and dephasing for each tone permits to determine the quality factors and eigenmodes frequencies, as well as the local complex driving force vector.

The interference pattern measured in reflection of the red probe laser, which is exploited to readout the nanowire vibrations presents positions (interference extrema) featuring no spatial gradient, which prevent from

correctly measuring the nanowire vibrations. It is important to properly estimate the local measurement vectors, but this may become delicate close to those extrema. In order to compensate for this potential source of errors, we have applied a local barycentric correction to the data: the force measurements are spatially averaged and weighted by the norm of the measurement vector magnitude:

$$F_i^{\mathrm{avg}} = \frac{\sum_{j=i-\Delta,i+\Delta} F_j|\beta_j|}{\sum_{j=i-\Delta,i+\Delta} |\beta_j|}$$

where F_i represents the force estimated at position i. We employed a sliding averaging over $2\Delta + 1$ neighboring points spreading over 25 nm. (Δ is adjusted depending on map grid). Fig. 14 illustrates this mechanism. The upper cure represents the cavity transmission, which permits identifying nodes and antinodes of the intracavity field, the bottom curve represents the norm of the measurement vector, which presents blind positions (marked by gray dashed lines). The central panel shows the force measured before (dots) and after (line) the barycentric correction. We note that due to the large signal to noise observed in our measurement conditions (force signal 20dB above the thermal noise and 60 dB above the background for 5 Hz resolution bandwidth), it is always possible to detect the driven force, even very close to the blind positions. The barycentric averaging thus serves to compensate for the errors arising in the evaluation of the measurement vectors close to the blind positions.

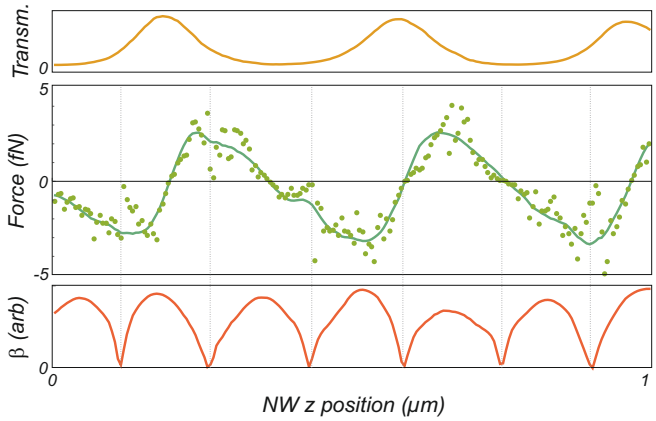

FIG. 14. **Correction for blind measurement positions in multi-frequency responses.** Illustration of the local barycentric smoothing employed in the data analysis to compensate for the reduction of readout sensitivity observed in the readout channel at the interference extrema. The cavity transmission is shown on top, while the bottom curves represents the norm of the measurement vector. Blind positions are marked by gray dashed lines. The central panel shows the force measured before (dots) and after (line) the local weighted averaging explained in the text.

Appendix C: Modeling

1. Orders of magnitude - Coarse estimation

The change in path length Δl accumulated in presence of the nanowire can be roughly evaluated as a geometric evaluation, where part of the vacuum is replaced by the nanowire dielectric. It can be expressed, when the nanowire of diameter d_{nw} is positioned in the middle of a gaussian beam of waist w_0:

$$\Delta l = (n_{SiC}-1)d_{\mathrm{nw}}\frac{2}{\pi w_0^2}\int_{-d_{\mathrm{nw}}/2}^{d_{\mathrm{nw}}/2} dx \int_{-\infty}^{\infty} dy \quad e^{-2(x^2+y^2)/w_0^2}.$$

So that the relative cavity path length change amounts to $\Delta l/L = 1.1 \times 10^{-3}$ for $d_{\mathrm{nw}} = 130\,\mathrm{nm}$, $w_0 = 1.7\,\mu\mathrm{m}$, $n_{\mathrm{SiC}} = 2.7$ and $L = 12\,\mu\mathrm{m}$. This order of magnitude is in good agreement with our measurements (see manuscript).

2. Model

We briefly describe here the ingredients employed in the model. It is based on a transmission matrix formulation, as standardly employed for membrane in the middle experiments [6, 7], with the difference that one has to describe a nanowire instead of a membrane.

The waist and the Rayleigh length of the cavity mode are determined by the cavity length, the mirrors curvature radii and by the laser wavelength. For simplicity, the cavity is assumed to be only resonant with the TEM_{00} Gaussian mode. In practice, cross-couplings between the different eigenmodes are easily obtained, and can be employed for enhancing quadratic coupling strength if needed, but the experimental results exposed in the article were obtained in a situation where no cross-couplings were observed. The cavity is pumped from the left side. Several approaches were employed to compute the transfer matrix of the nanowire, with different degrees of refinement (possibility of transverse coupling, description of the internal Mie resonances of the nanowire...). A simple approach is described below, which permits to understand most of the experimental signatures we have observed.

We assume that the nanowire dimensions are sufficiently small compared to the optical waist so that the incoming field presents wavefronts that are homogeneous over the nanowire extension and thus employ a "square" nanowire of lateral dimensions $L_{\mathrm{NW}} \times L_{\mathrm{NW}}$. To integrate the

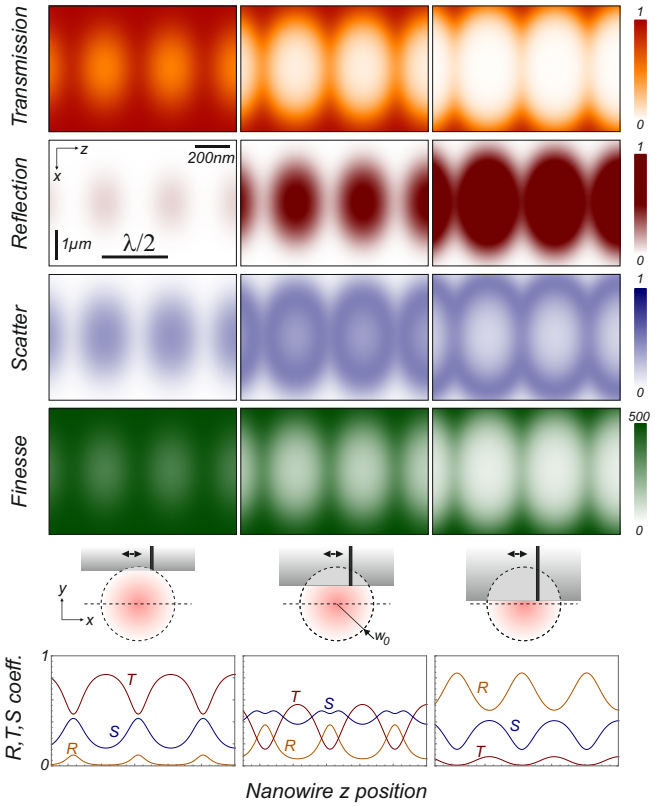

FIG. 15. **Typical results of simulations.** The transmitted, reflected and scattering coefficients, as well as the cavity finesse are computed for various positions of the nanowire in the XZ plane, and for 3 different vertical insertions in the mode volume (left to right: the nanowire bottom extremity is located at $1.8, 1, 0.2\,\mu$m above the optical axis (optical waist of $w_0 = 1.8\,\mu$m)). The other bare cavity properties are: 500 finesse, symmetric mirrors, $12\,\mu$m length

.

nanowire in the input-output formalism, we need to compute its effective reflection, transmission and loss coefficients. We thus define a nanowire effective layer with reflection and transmission coefficients that depends on $\mathbf{r}_\perp$, the transverse coordinate. When $\mathbf{r}_\perp$ belongs to the nanowire, these coefficients are taken identical to the reflection and transmission coefficients of the equivalent infinite layer with refractive index n and thickness $L_{\rm NW}$:

$$C_r = \frac{(1-n^2)\sin(nkL_{\rm NW})}{2in\cos(nkL_{\rm NW}) + (1+n^2)\sin(nkL_{\rm NW})}, \quad \text{(C1)}$$

$$C_t = \frac{2in}{2in\cos(nkL_{\rm NW}) + (1+n^2)\sin(nkL_{\rm NW})}. \quad \text{(C2)}$$

If $\mathbf{r}_\perp$ does not belong to the nanowire, we assume a plane wave propagation (which is valid for a nanowire close to the middle of the cavity) such as $C_r = 0$ and $C_t = \mathrm{e}^{ikL_{\rm NW}}$. Finally, the final reflection and transmission coefficients of the Gaussian beam through the

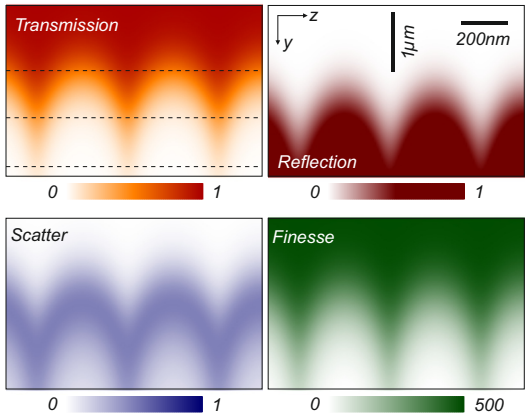

FIG. 16. **Typical results of simulations.** Same simulations as in Fig. 15 in the vertical YZ plane above the optical axis ($x = 0$). The optical axis is located at the bottom of the image, the 3 dashed lines corresponds to the NW elevations in the previous figure.

.

nanowire effective layer are obtained by assuming that the only part of the fields contributing to the intra-cavity field are the projections on the TEM_{00} mode, since it is the only one assumed to be resonant inside the cavity. They read as

$$t_{00}^{00} = \iint \mathrm{d}\,\mathbf{r}_\perp E_t(\mathbf{r}_\perp, Z_{\rm NW}) \left[E_{(+)}^{00}(\mathbf{r}_\perp, Z_{\rm NW})\right]^*, \quad \text{(C3)}$$

$$r_{00}^{00} = \iint \mathrm{d}\,\mathbf{r}_\perp E_r(\mathbf{r}_\perp, Z_{\rm NW}) \left[E_{(-)}^{00}(\mathbf{r}_\perp, Z_{\rm NW})\right]^*. \quad \text{(C4)}$$

where $E_{(\pm)}^{00}$ are the TEM_{00} normalized mode ($\iint \mathrm{d}\mathbf{r}_\perp |E_{(\pm)}^{00}(\mathbf{r}_\perp, z)|^2 = 1$) propagating along $\pm z$.

In practice the simulations are done in two steps. In a first time we compute the transfer matrix of the

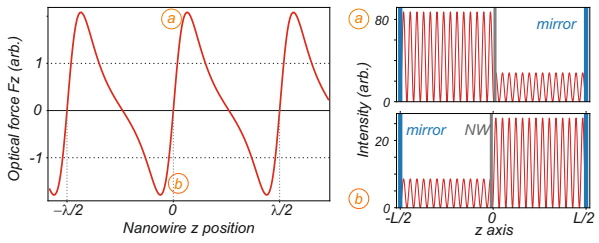

FIG. 17. **Simulations of the optical force profile.** Simulations of the optical axial force computed for different nanowire positions along the optical axis. The right panels illustrate the shape of the intensity distribution in the system for 2 positions of the oscillator, on the left and right sides of an optical node of the intracavity field. The left-right distributions of the field intensity in the 2 sub-cavities allows to understand the repulsive character of the force profile observed in the vicinity of optical nodes.

nanowire effective layer for all positions of the nanowire inside the cavity (both axially and vertically). Then, we use these transfer matrices to propagate the field through the system obtaining the transmission and reflection coefficients of the full cavity (see Fig.15,16). Using the energy conservation, we also extract the amount of light scattered out of the cavity due to the presence of the nanowire.
Those simulations are realized for different laser frequencies (or equivalently for different cavity lengths) in the vicinity of the system resonance which can be used to compute the strength of the parametric shifts of the cavity as well as modifications of its linewidth. Also, it is possible to track the cavity resonance to compute the optical signal or optical forces in presence of a cavity lock, as realized experimentally (Fig. 2de, Fig. 3-4).

Moreover we subsequently determine the field inside the two sub-cavities surrounding the nanowire (see Fig.17). Once the fields around the nanowire are known, we can estimate the optical force exerted by the intracavity field on the nanowire, and in particular its impact on the dynamics of the 2 transverse fundamental eigenmodes of the nanowire. To do so one needs to convolve the optical force density with the eigenmode deformation profile. Since the optical field is essentially located close to its vibrating extremity, where the eigenmodes deformation profiles are locally uniform and can be assimilated to a simple translation on the extent of the optical waist, the effect of the optical forces can be assimilated to the integral of the Maxwell stress tensor on the nanowire surface. We can then, assuming a nanowire positioned on the cavity axis, compute the optical force along z applied by the intra-cavity field on the nanowire for different positions and cavity properties.
Fig.17 shows a typical result of the axial force field pattern measured for varying positions along the optical axis obtained with this modeling (square nanowire of 115 nm dimensions). The right panels illustrate the spatial profiles of the electromagnetic field intensity in the system, for 2 positions of the oscillator on the left and on the right of a node. For both positions the parametric shift is identical, but the optical force changes sign. This can be explained by the different amount of light stored in the left/right sub-cavities. Furthermore, the positive/negative asymmetry observed in the force profile is due to the asymmetric pumping conditions: it is easier to pump the left cavity compared to the right cavity when the system is pumped from the left hand side. In those simulations both mirrors were taken identical, in practice, this asymmetric behavior also depends on the mirrors reflectivities.
The simulated and experimentally measured force fields are observed to be very repulsive in the vicinity of the optical nodes (large slopes), but respectively less attractive towards the optical anti-nodes (smaller inverse slopes) even if the parametric coupling strength G_z presents the same magnitude at both positions. This is a consequence of the reduction of the cavity finesse observed when the nanowire enters the scatter rings visible in the scatter maps: the intracavity field thus benefits from a lower cavity enhancement, thus reducing the magnitude of the optical force exerted on the nanowire.

Appendix D: Intracavity photon number

The intracavity photon number employed in the response measurements are experimentally deduced using the input output formalism, modeling the overall nanowire in the middle (NIM) system as an equivalent dual port 1D optomechanical system with an input mirror of transmissivity T (in intensity) and a back mirror featuring a transmissivity P (taking into account the second mirror transmissivity as well as the nanowire induced optical losses). The intracavity photon number N is related to the intracavity photon flux I (in photon/s) by: $I = N/(2L/c)$ where $2L/c$ is the photon round trip duration in the cavity, while the latter is related to the input photon flux $I_{\rm in} = P_{\rm in}/h\nu$ by: $I = I_{\rm in}\frac{4T}{(T+P)^2}$, in case of a perfect injection efficiency. The cavity finesse is connected to the overall cavity losses by $\mathcal{F} = 2\pi/(T+P)$. In our experiment, the injection efficiency η is limited by the fiber injection efficiency (80% including splices and fiber connector losses) and the mode matching from the fiber to the cavity fundamental mode (70%) to an overall value of $\eta = 0.56$. The connection between the incoming power $P_{\rm in}$ and the intracavity photon number is thus given by:

$$N = \eta\frac{2L}{\pi c}\mathcal{F}\frac{2T}{T+P}\frac{P_{\rm in}}{h\nu} = \eta\frac{2L}{\pi^2 c}\mathcal{F}^2 T\frac{P_{\rm in}}{h\nu}.$$

The cavity parameters (T, P) are deduced from optical measurements of the cavity finesse realized by scanning the cavity length around a resonance. In absence of the nanowire, we operate with a symmetric cavity ($P = T$), while the cavity external losses P are increased in presence of the nanowire, and are computed in each position. In Fig. 3abcd, at the position where the response linearity was verified, a modulation of the input power of 100 nW generates a modulation of the intracavity photon number of 0.6 ($\mathcal{F} = 202$, $4T/(T+P) = 1.05$, $L = 12\,\mu$m), so that we can largely detect modulations of the mean intracavity photon number smaller than unity.

The advanced numerical simulations [8] of the system, see Fig.18, show that this assimilation of the NIM setup to an equivalent 1D optomechanical system is valid to estimate the intracavity photon number in the case of a response measurement where the system is pumped from one single port. In this approach, after having evaluated

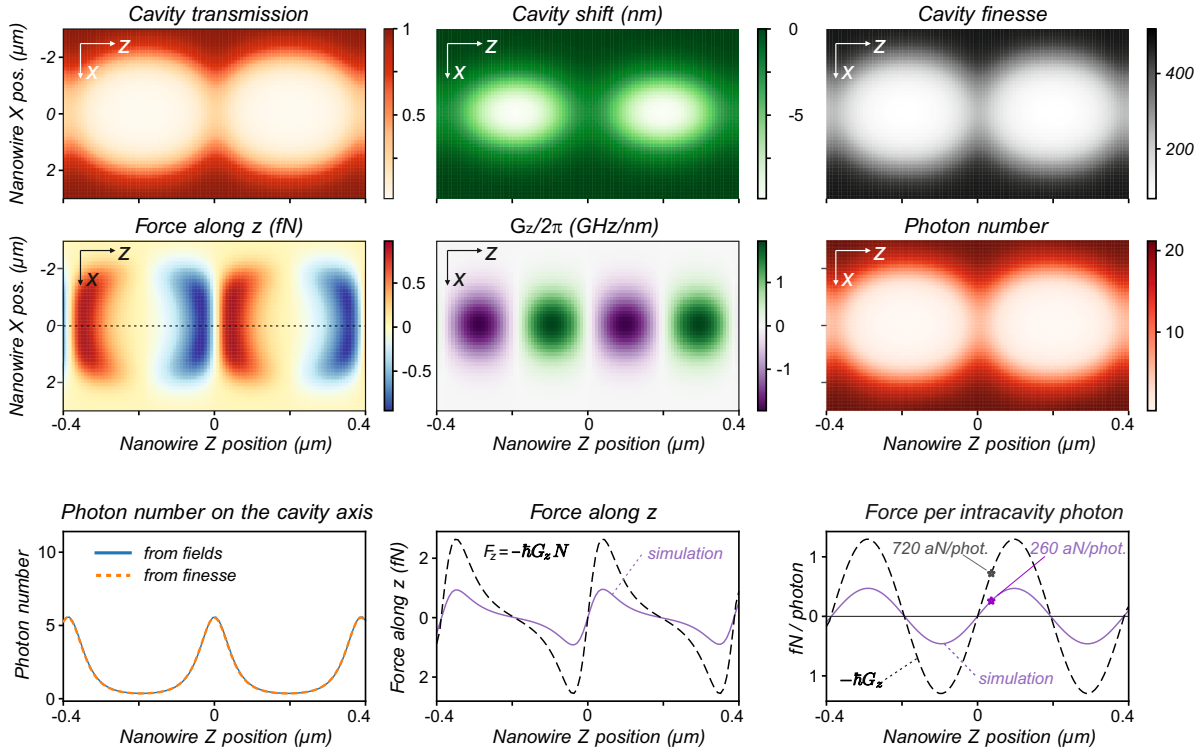

FIG. 18. **Numerical simulations of the experiment.** Results of the complete simulation [8] of the experiment, accounting for internal Mie resonances in the nanowire. Parameters employed are $L_{\rm cav} = 12\,\mu$m, $R_{\rm nw} = 65$ nm, radius of curvature of the mirrors : $28\mu m$, mirrors reflectivities: 0.994, perpendicular polarization, wavelength: $\lambda = 770$ nm, input power: $P_{\rm inc} = 400$ nW with perfect mode matching. The lower panels are slices taken along the optical axis.

the intracavity fields, the photon number is deduced by computing the overall energy stored in the optical resonator, and dividing it by the energy of a single photon ($h\nu$). The numerical simulations also permit to estimate the expected force per intracavity photon change, at the level of 260 aN/photon, whose magnitude is in good agreement with our measurements (340 aN/photon). We underline that the model employed here assumes that the nanowire optical response can be assimilated to the one of an infinite cylinder (so that the description of light scattering in the framework of Mie scattering remains analytical), inserted perfectly transversally to the optical mode. In practice, we operate in general only a few microns above the nanowire tip, which may not be sufficiently far away from the tip, and we often suffer from a residual tilt (typically a few degrees) of the nanowire with respect to the optical axis. Finally, the delicate estimation of the optical pumping efficiency will always remain one of the most important source of discrepancy between our measurements and the ideal predictions of the model.

In both theoretical and experimental cases, those single photon forces are comparable but about 0.4 times smaller than the value of $F^{(1)}$ expected from the coupling strength g_0. The understanding of the origin of this slight discrepancy and the modeling of the contribution of all the other vacuum modes (Casimir forces) will be the subject of future work.

Appendix E: Observing quantum radiation pressure noise at the single photon level

The goal of this section is to derive, in the semi-classical framework, a dynamical criterion comparing the impact of the radiation pressure force fluctuations $\delta F_{\rm i}$ and of the thermal fluctuations $\delta F_{\rm th}$ on the oscillator dynamics in an optomechanical system. For that purpose we consider the simple case of a high finesse and single port optical cavity pumped by a monochromatic laser, where the second mirror can oscillate around its equilibrium position. Following the methodology of ref.[9], the oscillator displacement in frequency space is shown to be

$$\delta x[\Omega] = \chi_{\rm eff}[\Omega]\big(\delta F_{\rm th}[\Omega] + \delta F_{\rm rad}[\Omega]\big), \qquad \text{(E1)}$$

where $\chi_{\rm eff}$ is the effective susceptibility of the oscillator dressed by the light verifying $\chi_{\rm eff}[-\Omega] = \chi^*_{\rm eff}[\Omega]$. The expression of the radiation pressure force fluctuations is

$$\delta F_{\rm rad}[\Omega] = 2\hbar k\,|\bar{\alpha}|\sqrt{\frac{2\gamma}{\gamma^2+\bar{\Psi}^2}}\left(\frac{\gamma^2+\bar{\Psi}^2-i\gamma\Omega\tau}{(\gamma-i\Omega\tau)^2+\bar{\Psi}^2}\,\delta p_{\rm in}[\Omega]-i\frac{\bar{\Psi}\Omega\tau}{(\gamma-i\Omega\tau)^2+\bar{\Psi}^2}\,\delta q_{\rm in}[\Omega]\right), \tag{E2}$$

where $\delta p_{\rm in}$ and $\delta q_{\rm in}$ are the quadratures of the intensity and phase fluctuations which will be set to one since in the following we consider a cavity pumped with a coherent state. In Eq. (E2), k is the wavevector of the light, $|\bar{\alpha}|^2$ the intra-cavity photon flux, $\gamma \ll 1$ characterizes the cavity losses ($r = 1-\gamma$, $t \simeq \sqrt{2\gamma}$), $\tau = 2L/c$ is the intra-cavity round trip time, and $\bar{\Psi}$ is the cavity-laser detuning.

Since $\delta F_{\rm rad}$ and $\delta F_{\rm th}$ are uncorrelated, the position noise spectrum reads as

$$S_{\delta_x}[\Omega] = |\chi_{\rm eff}[\Omega]|^2\,\left(S_{\delta F_{\rm rad}}[\Omega] + S_{\delta F_{\rm rad}}[\Omega]\right), \tag{E3}$$

so that the quantum radiation pressure noise will dominate if the following criteria is fulfilled:

$$\eta_{\rm rad} \equiv S_{\delta F_{\rm rad}}[\Omega]/S_{\delta F_{\rm th}}[\Omega] > 1 \tag{E4}$$

In the case of an adiabatic cavity ($\Omega_m \ll \Omega_c$, Ω_c being the cavity cut-off frequency), the noise spectral density of the optical force is given by

$$S_{\delta F_{\rm rad}}[\Omega] = \frac{8\hbar^2k^2\,|\bar{\alpha}|^2\,\gamma}{\gamma^2+\bar{\Psi}^2}, \tag{E5}$$

while the Langevin noise spectral density is $S_{\delta F}[\Omega] = 2M\Gamma_{\rm m}k_BT$ where M is the effective mass of the oscillator, $\Gamma_{\rm m}$ its decoherence rate and T the temperature of the bath. At the optical resonance ($\bar{\Psi} = 0$), the dynamic criterion becomes

$$\eta_{\rm rad} = \frac{4\hbar^2k^2\,|\bar{\alpha}|^2}{M\Gamma_{\rm m}k_BT\gamma} \tag{E6}$$

where $|\bar{\alpha}|^2 = Nc/2L$ is expressed in terms of the intra-cavity photon number N and of the cavity length L (c being the light velocity). Using $\gamma/k = \kappa/G$ and $L/k = 1/G$ with $G = \omega/L = \partial_x\omega$ the optomechanical coupling strength of the system, we get

$$\eta_{\rm rad} = 2NC^{(1)}\,\frac{Q}{n_T} \tag{E7}$$

where we have also used $g_0 = G\delta x_{\rm zpf}$ and the expression of the single photon optomechanical parametric cooperativity $C^{(1)} \equiv 2g_0^2/\kappa\Omega_m$ introduced in the manuscript. In Eq. (E7), $n_T \equiv k_BT/\hbar\Omega_m$ is the initial thermal phonon number and $Q = \Omega_m/\Gamma_{\rm m}$ is the nanowire quality factor respectively. In the case of an adiabatic cavity, the later is only weakly affected by the optomechanical effects, and can be assimilated to its value in absence of light.
When the system is bistable at the single photon level, $C^{(1)} > 1$, the dynamical criteria simply requires $Q > n_T/2$. Both conditions would be fulfilled if one could reproduce the present experiment in a dilution fridge, using the nanowires already employed in such a cold environment [3]: $2Q/n_{\rm T}$ ratios above 2.5 were already achieved, while cooperativities larger than 10 can be envisioned. This is a challenging but feasible experiment, and the orders of magnitude are clearly encouraging.

[1] Gloppe, A. *et al.* Bidimensional nano-optomechanics and topological backaction in a non-conservative radiation force field. *Nat. Nanotechnol.* **9**, 920 (2014).

[2] Mercier de Lépinay, L. *et al.* A universal and ultrasensitive vectorial nanomechanical sensor for imaging 2D force field. *Nat. Nanotechnol.* **12**, 156 (2016).

[3] Fogliano, F. *et al.* Ultrasensitive nano-optomechanical force sensor at dilution temperatures. *Arxiv:2009.02912* (2020).

[4] Leijssen, R., La Gala, G. R., Freisem, L., Muhonen, J. T. & Verhagen, E. Nonlinear cavity optomechanics with nanomechanical thermal fluctuation. *Nat. Commun.* **8**, 16024 (2017).

[5] Mercier de Lépinay, L., Pigeau, B., Besga, B. & Arcizet, O. Eigenmode orthogonality breaking and anomalous dynamics in multimode nano-optomechanical systems under non-reciprocal coupling. *Nat. Commun.* **9**, 1401 (2018).

[6] Jayich, A. M. *et al.* Dispersive optomechanics: A membrane inside a cavity. *New J. Phys.* **10**, 1 (2008).

[7] Reinhardt, C., Müller, T., Bourassa, A. & Sankey, J. C. Ultralow-noise sin trampoline resonators for sensing and optomechanics. *Phys. Rev. X* **6**, 021001 (2016).

[8] Reigue, A. *et al.*. Cavity nano-ptomechanics with suspended nanowires: modelisation and novel phenomenology. *in preparation* (2020).

[9] Fabre, C. *et al.* Quantum-noise reduction using a cavity with a movable mirror. *Phys. Rev. A* **49**, 1337 (1994).